Optimized Nickel-Cobalt and Nickel-Iron Oxide Catalysts for the Hydrogen Evolution Reaction in Alkaline Water Electrolysis

Alaa Y. Faid,[1,*] Alejandro Oyarce Barnett,[2] Frode Seland,[1,] and Svein Sunde[1,**,z]**

[1]*Department of Materials Science and Engineering, Norwegian University of Science and Technology (NTNU), Trondheim, Norway*
[2]*SINTEF Industry, Sustainable Energy Technology Department, New Energy Solutions, Trondheim, Norway*

Ni and Ni-doped with transition metals (TM) such as Fe and Co represent the most suitable electrodes for hydrogen evolution reaction (HER) in alkaline media. Various compositions of co-precipitated $Ni_{1+x}Fe_{2-x}O_4$ and $Ni_{1+y}Co_{2-y}O_4$ nanoparticles were investigated. The intrinsic HER catalytic activity is the same for all the catalysts, which we relate to similar values of the iso-electric point (IEP). However, the mass catalytic activity of the catalysts changes through a modification of the electrochemical surface area. Fractional reaction orders for hydrogen evolution revealed in all catalyst compositions are due to double layer effects and surface acid-base equilibria. Reaction order and Tafel slope of the catalysts are compatible with electrochemical adsorption as the rate-determining step for the HER. Tafel slopes were also evaluated independently from impedance spectroscopy, in good agreement with the polarization curves. Electrodes prepared from catalyst inks containing an anion-exchange ionomer displayed inferior catalytic activity for the HER as compared to electrodes prepared with Nafion in the ink. Chronoamperometry confirmed the sustained superior hydrogen kinetics over time of $NiFe_2O_4$ and $NiCo_2O_4$ composition over that of NiO.
 [DOI: 10.1149/2.0821908jes]

Manuscript submitted February 12, 2019; revised manuscript received April 22, 2019. Published May 8, 2019. This was Paper 1806 presented at the Seattle, Washington Meeting of the Society, May 13–17, 2018.

The Polymer Electrolyte Membrane electrolyzer (PEMEL) has attracted considerable attention during the last decades.[1] Some of the advantages of PEM electrolysis are high current densities, low parasitic energy losses, rapid power-up/power-down rates, and high purity and high-pressure hydrogen.[2] PEMELs are therefore promising devices for production of hydrogen for energy storage and subsequent use in the transport sector.[1,2] The low pH associated with PEM devices results in active hydrogen evolution reaction (HER) at the cathode, but the overpotential at the anode at the low pH associated with PEMELs is very large unless catalysts based on very expensive and scarce elements such as iridium are employed. Although the overpotential for the oxygen evolution reaction (OER) at the anode is significant also under alkaline conditions, the overall electrode kinetics tend to favor an alkaline environment.[1,3,4] Alkaline water electrolyzers operating at a high pH represent the standard and traditional technology for large-scale, industrial water electrolysis.[3]

The overpotentials associated with the HER at high pH have been reported to be exceptionally high compared those at low pH, and correspond to a hundred-fold decrease in activity at Pt, Ir, and Pd.[4] The reason for the lower activity has, among other things, been suggested to be a stronger bond between the hydrogen and the metal surface under alkaline conditions.[3,5] According to this view the primary descriptor of catalytic activity under alkaline conditions is the hydrogen binding energy.[3] Associating the catalytic activity for the HER with the hydrogen binding energy would make the catalysts subject to rational design guided by the d-band theory for transition metal electrocatalysis.[4]

Recent developments in anion exchange membrane (AEM) technology have led to the possibility of using anion-exchange membranes containing alkaline ions (OH^-, CO_3^{2-}, HCO_3^{2-}) in water electrolysis.[6] AEM technology has the potential of combining the advantage of non-precious catalysts of the traditional alkaline process, with the benefits of PEMEL such as fast power-up/power-down rates, low parasitic energy losses, and low energy consumption, in other words consolidating the best of both technologies.[7]

Electrocatalysts based on transition metal oxide (TMOs) are cheap, environmentally benign, and active OER catalysts in alkaline environments.[8] Development of cheap transition metal-based alkaline HER catalysts will reduce the cost of the electrolysis operation, which is beneficial for overall water splitting application.[8] Ni and Ni alloys with (Fe,Co,Mo) are considered as the best electrode materials for HER in alkaline environments.[9] The fundamentals of the hydrogen evolution mechanism on transition metals is, however, still unclear.[10]

In addition to the catalytic action of the transition metal or metal oxide, its interaction with the ionomer may play a role.[11] The ionomer acts as a stabilizing and binding agent in catalyst-solvent inks. A major function of the ionomer in the catalytic layer in a water electrolyser is to promote ink uniformity and coating quality. Modestino et al.[12] showed that the degree to which the ionomer wets the catalyst in thin-film catlytic layers can drastically affect the internal morphology of the polymer and in turn influence electrochemical activity. If the AEM water electrolyzer is fed with pure water or with an electrolyte of low concentration, the ionomer may also be important in providing ionic conductivity in the layer and expanding the reaction zone.[12]

There are two crucial drawbacks associated with Ni-based electrodes in alkaline electrolyzers; the first being a high operating cell voltage, and the second is the decrease in cathodic activity with time. The type of polymer/catalyst system and their interaction could have major implications for the for the HER.[13] It thus remains a challenge to optimize active, stable, and cheap HER catalyst for AEM water electrolysis.

In this work, a detailed study has been carried out on $Ni_{1+x}Fe_{2-x}O_4$ and $Ni_{1+y}Co_{2-y}O_4$ oxide catalysts with x and y in the range $-1, \ldots, 1$. For reference we have also included the pure nickel oxide catalyst (NiO). Investigation of the effect of composition on structural properties is based on the analysis of surface morphology, crystalline phases, and BET surface area. The relationship between the composition of nanoparticles and the catalytic activity for HER is illustrated. The reaction order at constant ionic strength has been investigated to reveal the mechanism of hydrogen evolution. This work also studies the influence of ionomer type on HER activity. We have used electrochemical impedance spectroscopy (EIS) as an additional method to evaluate hydrogen evolution kinetics at the electrode-electrolyte interface. Stability and durability were assessed by chronoamperomtery measurements for 24 hours.

Experimental

Preparation of the catalyst.—Catalyst nanoparticles containing Ni, Ni and Fe, and Ni and Co were fabricated by the co-precipitation method reported by Chanda et al.[11] with some minor modifications. Appropriate molar concentrations of as-received $Ni(NO_3)_2 \cdot 6H_2O$ (purity <97%, Sigma-Aldrich), $FeCl_3 \cdot 6\,H_2O$ (purity <99.9%,

*Electrochemical Society Student Member.
**Electrochemical Society Member.
zE-mail: svein.sunde@ntnu.no

Table I. Compositions of the nickel-iron and nickel cobalt oxide catalysts investigated.

Ni/Fe or Ni/Co	mole-% Ni	mole-% Fe or Co	$Ni_{1+x}Fe_{2-x}O_4$	$Ni_{1+y}Co_{2-y}O_4$
0	0	100	Fe_3O_4	Co_3O_4
0.1	9	91	$Ni_{0.27}Fe_{2.73}O_4$	$Ni_{0.27}Co_{2.73}O_4$
0.33	25	75	$Ni_{0.74}Fe_{2.26}O_4$	$Ni_{0.74}Co_{2.26}O_4$
0.50	33	67	$NiFe_2O_4$	$NiCo_2O_4$
0.75	43	57	$Ni_{1.29}Fe_{1.71}O_4$	$Ni_{1.29}Co_{1.71}O_4$
∞	100	0	NiO	NiO

Sigma-Aldrich), and $Co(NO_3)_2{\cdot}6\,H_2O$ (purity <98%, Sigma-Aldrich) were dissolved in 150 mL of deionized (DI) water under stirring for 15 min. Then 2 mol dm^{-3} NaOH (Sigma aldrich 99.99% trace metals basis) solution was added under continuous stirring until a precipitate formed. Precipitation occurred when the pH of the reaction mixture reached values higher than 12. The solution was stirred for another hour at room temperature (22 ± 2°C) and left to stand for 12 hours. The precipitated solution was filtered, washed with DI water and dried at (80°C). The hydroxide precipitate was moved to a crucible and calcinated at (500°C) for four hours under a reducing 5% H_2/95% Ar atmosphere. Finally, the powders were crushed in a mortar.

We will show below in Table I that the cobalt- and iron-containing catalysts manufactured here are oxides and possess the spinel structure. We will therefore refer to these below as $Ni_{1+x}Fe_{2-x}O_4$, or $Ni_{1+y}Co_{2-y}O_4$, with x ranging from $x = -1$ to $x = 1$. The pure Ni sample will be shown to be NiO (with the rocksalt structure), and will be designated as such.

Surface and morphological characterization.—The morphology of the prepared powder samples was studied using scanning electron microscopy (SEM, Carl Zeiss supra 55) operated at a 10-kV accelerating voltage and Hitachi S-5000 FE-SEM. Elemental analysis was carried out using energy dispersive spectroscopy (EDS) in SEM (Carl Zeiss supra 55). Structural and phase characteristics of the catalyst were obtained using a Bruker D8 A25 DaVinci X-ray Diffractometer with $Cu-K_\alpha$ radiation. The wavelength of the radiation was 1.5425Å. X-ray diffraction (XRD) patterns were recorded in the 2θ-range 15 through 75 and with a step size of 0.3 (2θ). Raman spectroscopy was performed with a Renishaw InVia Reflex Spectrometer System using visible-light excitation at 532 nm (100 mW) with a spectral resolution < 1 cm^{-1} at room temperature (22 ± 2°C). Catalyst specific surface area was determined using the Brunauer-Emmett-Teller method (BET) of nitrogen adsorption using a TRISTAR 3000 surface area and porosity analyzer. The dried samples were degassed at 250°C under vacuum overnight before the measurement. The zeta potential of the nanoparticles was measured using a Beckman Coulter Delsa Nano C (Beckman Coulter, Inc). The device was kept at constant temperature, 25°C. Ten-fold diluted suspensions of nanoparticles were used in the measurement. The device measures the zeta potential at five different cell positions (0.7, 0.35, 0, −0.35, −0.7) to exclude the influence of Brownian motion. The pH of the suspensions was adjusted by small additions of a 1 mol dm^{-3} HCl or KOH solution.

Electrocatalytic measurements.—Linear sweep voltammetry (LSV) was performed using a multi-channel electrochemical potentiostat (Ivium-n-Stat). A conventional three-electrode arrangement was applied in an alkaline resistant PTFE cell (PINE research). A rotating disk electrode (RDE) (PINE MSRX rotator, PINE Research Instrumentation, USA) was used as the working electrode; a platinum foil served as the counter-electrode. A standard single junction mercury/mercury oxide (Hg/HgO) electrode filled with a 4.24 mol dm^{-3} KOH solution was used as a reference electrode.

For the RDE experiments, a catalyst ink was prepared by mixing 5 mg of catalyst powder in a solution of (0.5 ml D.I water, 0.44 ml isopropanol (Sigma Aldrich) and 0.06 ml (5 wt%) Nafion 117 solution(Sigma Aldrich). The ink solution was ultrasonicated for 30 minutes. To investigate the electrocatalytic activity, an aliquot of 10µl of catalyst ink deposited on a polished glassy carbon (GC) disk electrode rotating at 200 rpm. The ink was subsequently dried in air at room temperature by maintaining the rotator speed at 700 rpm for 30 min. The effect of the binder type was investigated by employing Fumion FAA-3 ionomer (a commercial polymer with quaternary ammonium groups providing the anion exchange function, supplied by Fumatech GmbH) instead of Nafion.

The LSV curves were collected in a potential range of −0.8 through −1.9 V vs. Hg/HgO using a 5 mV s^{-1} scan rate at 1600 rpm rotation rate. All electrochemical experiments were carried out at a temperature of 22 ± 2°C. All electrolyte solutions were prepared with deionized water (Millipore Direct-Q3). N_2 gas purged the freshly prepared 0.1 mol dm^{-3} KOH alkaline electrolyte for 30 minutes before the electrochemical measurements. All resulting data were corrected for omhmic polarization due to the solution resistance (to 85 %) during the measurement. The potential was corrected for ohmic resistance through the equation

$$E_c = E_m - iR \quad [1]$$

where E_c is compensated potential, E_m is the measured potentials, i is the current produced, and R is ohmic resistance.

Reaction order measurements were carried out at four different pH values. The nominal pH values of the electrolytes were 14, 13, 12 and 11. The ionic strength kept constant by the addition of $NaClO_4$ (monohydrate, Aldrich, ACS reagent 98%) to solutions of pH value lower than 14. To make the electrolyte solutions of equal ionic strength, y mol dm^{-3} KOH and [1 - y] M $NaClO_4$ was used. The pH of the solutions was measured with a pH-meter (pHep 5: pH/Temperature tester- with 0.01 pH resolution, Hanna Instruments). The same ink formulation as above was used for these experiments also, but without Nafion or any other binder to avoid any influence of the binder on the local pH.[48] The ink stability on the electrode in the absence of a binder was maintained by using a low mass loading of 250 µg cm^{-2}. To obtain quasi-steady state polarization curves, the electrode was kept at 10 min at open-circuit potential, then at −1.2 V vs. Hg/HgO for 30 minutes followed by recording of polarization curves at 20 mV s^{-1} to demonstrate a stable polarization response.[14] The liquid junction potential between the electrolyte solution and the inner solution of the reference electrode was reduced as much as possible by keeping the KOH concentration in electrolyte and filling solution inside the reference electrode the same. The data shown were compensated for 85% of the ohmic resistance as above. The liquid junction potentials were estimated from the Henderson equation[15] at all pH for which all measurements were corrected. The values of liquid junction potentials were 6, 4, 3, and 2 mV for pH values 14, 13, 12, and 11 respectively.

The electrochemical impedance of the electrodes were measured at frequencies in the range 0.01 Hz through 100 kHz with a 10 mV sinusoidal voltage perturbation in 0.1 mol dm^{-3} KOH at different applied potentials. Short-term stability tests were carried out using chronoamperometry for 24 hours at −350 mV constant cathodic overpotential. All potentials measured were converted to potentials as they would have been measured with a reversible hydrogen electrode (RHE) through

$$E_{RHE} = E_{Hg/HgO} + 0.098\ V + 0.059\ V \times pH \quad [2]$$

where E_{RHE} is the potential vs. the RHE, and $E_{Hg/HgO}$ is the measure potential.

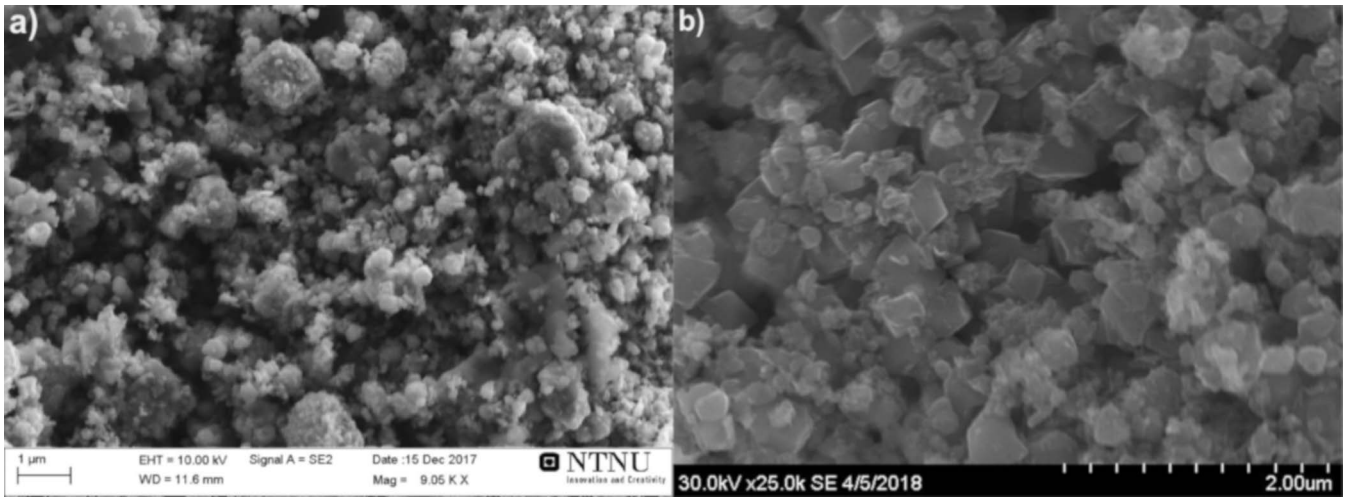

Figure 1. SEM image of a) $Ni_{1+x}Fe_{2-x}O_4$ with 33 mole-% Ni and b) $Ni_{1+y}Co_{2-y}O_4$ with 33 mole-% Ni prepared by co-precipitation.

Results and Discussion

Surface morphology and structural characterization.—Figure 1 displays SEM images of the surface morphology of nanoparticles of a) $NiFe_2O_4$ (33 mole-% Ni) and b) $NiCo_2O_4$ (33 mole-% Ni) prepared by the co-precipitation method and calcined at 500°C for four hours under 5% H_2/ 95 % Ar atmospheres. The images in Figure 1 were collected prior to the crushing step (see Experimental). From the SEM images we estimate the size of the produced nanoparticles to be in the range 150 through 200nm. The particles are agglomerated, possibly during the calcination step of the preparation procedure. The agglomeration can be seen clearly in Figure 1, and is the reason for including a crushing step as a part of the catalyst preparation. Similar results were reported by Chanda et al.[11]

Energy dispersive X-ray spectroscopy (EDX) was recorded to investigate the elemental composition of the sample. Figure 2 shows EDX results for NiCo and NiFe oxides with 33 mole-% Ni. Table II shows the weight-% of Ni, Fe, Co, and O as measured by energy dispersive X-ray spectroscopy for the various compositions of $Ni_{1+x}Fe_{2-x}O_4$, $Ni_{1+y}Co_{2-y}O_4$, and NiO nanoparticles. The EDX analysis confirms that the prepared nanoparticles consist of Ni, Fe, and O, and Co, Ni, and O respectively, without any incorporation of NO_3^- or Cl^- salts.

According to the literature the formation of nanoparticles by co-precipitation involves hydroxide formation and then dissociation to oxide.[16] For example for $NiCo_2O_4$ the sequence of reactions may be written as

$$Ni(NO_3)_2 \cdot 6\,H_2O(s) + 2\,Co(NO_3)_2 \cdot 6\,H_2O(s) + 6\,KOH(aq) \longrightarrow Ni(OH)_2(s) + 2\,Co(OH)_2(s) + 6\,KNO_3(aq) + 12\,H_2O \quad [3]$$

$$Ni(OH)_2(s) + 2\,Co(OH)_2(s) + \frac{1}{2}O_2 \longrightarrow NiCo_2O_4(s) + 3\,H_2O(\ell) \quad [4]$$

Figure 3a shows diffraction patterns for all compositions of the $Ni_{1+x}Fe_{2-x}O_4$ series of catalysts. For the samples with 33 and 43 mole-% Ni, diffraction peaks at 2θ equal to 30.11°, 35.57°, 43.11°, 48.20°, 53.33°, 57.11°, and 63.21° are apparent. These can be attributed to

Table II. Overview energy dispersive X-ray (EDX) results of elemental weight-% for nanoparticles of $Ni_{1+x}Fe_{2-x}O_4$, $Ni_{1+y}Co_{2-y}O_4$, and NiO synthesized by co-precipitation. (In the table "wt-%" refers to the weight percent.)

Ni/Fe or Ni/Co	mole-% Ni	wt-% Ni	wt-% F	wt-% Co	wt-% O
0	0	0	42		58
0.1	9	8	70		22
0.33	25	19	57		24
0.5	33	27	50		23
0.75	43	34	44		22
∞	100	48	0	0	52
0	0	0		43	57
0.1	9	9		68	23
0.33	25	18		59	23
0.5	33	27		51	22
0.75	43	35		44	21

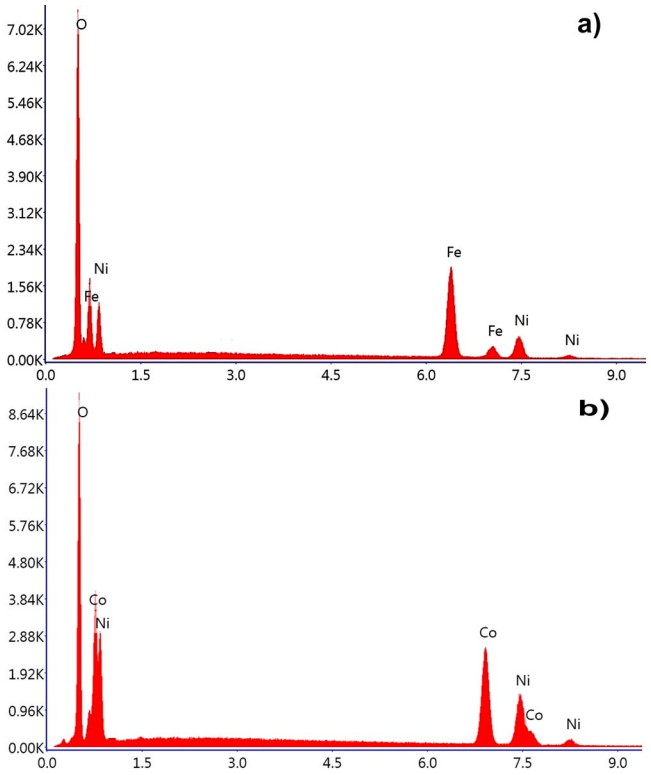

Figure 2. EDX Spectrum of a) $Ni_{1+x}Fe_{2-x}O_4$ with 33 mole-% Ni and b) $Ni_{1+y}Co_{2-y}O_4$ with 33 mole-% Ni prepared by co-precipitation.

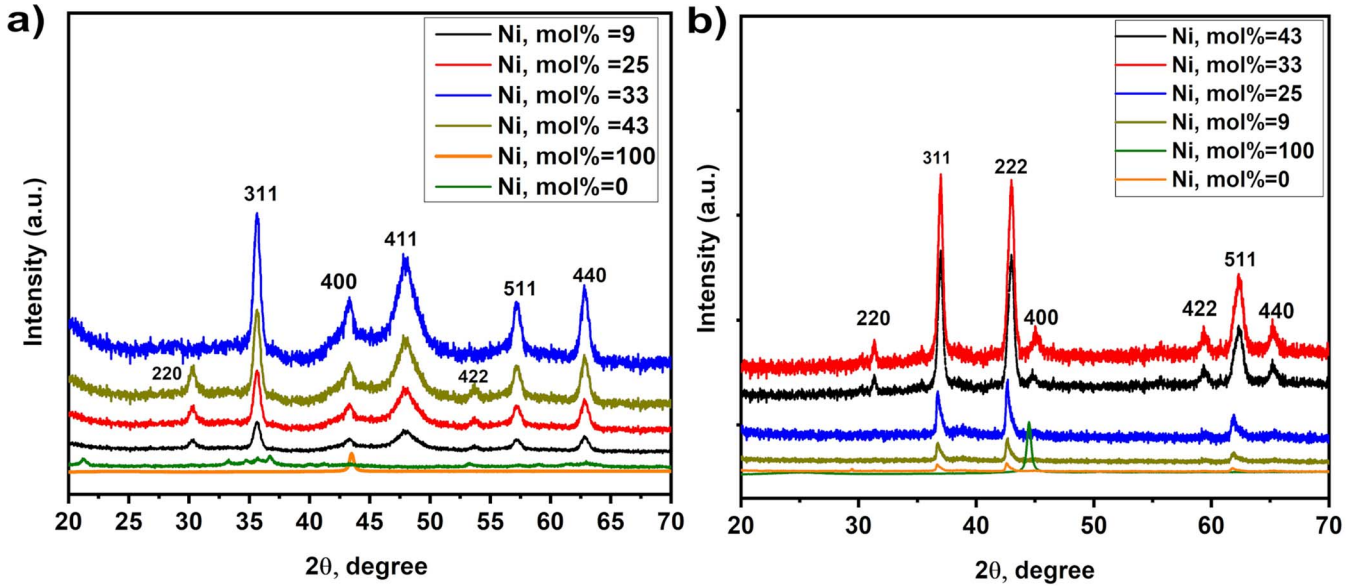

Figure 3. XRD patterns of a) $Ni_{1+x}Fe_{2-x}O_4$ and b) $Ni_{1+y}Co_{2-y}O_4$ nanoparticles with different mole-% Ni compositions prepared using co-precipitation with NaOH as precipitating agent and annealing in reducing atmosphere 5% H_2 / 95% Ar at 500°C for 4 hours.

indices (220), (311), (400), (411), (422), (511), and (440), respectively, for the spinel crystal structure of $NiFe_2O_4$ (JCPDS card NO.86-2267).[17] Similar patterns are apparent for the other $Ni_{1+x}Fe_{2-x}O_4$ compositions, but with some of the diffraction peaks being a little less pronounced. For example, the peak corresponding to index (220) is not clearly visible in the diffraction pattern for 9 and 25 mole-% Ni. However, the XRD patterns in Figure 3a strongly indicates that all $Ni_{1+x}Fe_{2-x}O_4$ samples are of the spinel type.

For Ni=100 mole-% (NiO) particles, the diffraction peak is appearing at $2\theta = 43.3°$. This can be indexed to (200) reflection of the face-centered cubic (*fcc*) of rock-salt NiO.[18] The XRD pattern of 0 mole-% Ni (Fe_3O_4) nanoparticles is shown in Figure 3a. Peaks at 2θ equal to 32.32°, 35.40°, 43.38°, 53.36°, and 63.12° are visible. These peaks can be indexed to indexes (311), (222),(422), (511), and (440), respectively, for the crystal structure of Fe_3O_4 compatible with JCPDS card NO.19-0629.[19]

Figure 3b displays diffraction patterns of $Ni_{1+y}Co_{2-y}O_4$ nanoparticles. For 33 mole-% Ni ($NiCo_2O_4$) and 43 mole-% Ni ($Ni_{1.29}Fe_{1.71}O_4$), the peak positions are appearing at 2θ value of 18.98°, 31.27°, 36.91°, 44.17°, 45.20°, 59.35°, 62.30°, and 64.82°. These diffraction peaks can be indexed as (111), (220), (311), (222), (400), (422), (511), and (440) crystal planes cubic spinel structure of $NiCo_2O_4$ with JCPDS card NO.73-1702.[8] XRD patterns in Figure 3b clearly show the development of (220) and (400) reflections when the mole-% Ni exceeds 33.

For 0 mole-% Ni with Co (Co_3O_4) exhibits diffraction peaks with 2θ values of 29.37°, 37.02°, 43.57° and 64.44°. These diffraction peaks can be indexed to the crystalline cubic spinel phase Co_3O_4 with JCPDS Card No.76-1802.[18]

The crystallite size of the co-precipitated nanoparticles was calculated using Scherrer equation based on full width of half maximum (FWHM):

$$t = \frac{0.9\,\lambda}{B\,\cos\theta} \qquad [5]$$

where t is the crystallite size, λ is the wavelength, B is the full width at half maximum of the peak, and θ is the peak diffraction angle. Table III shows crystallize size (nm) as function of the mole-% Ni in NiFe and NiCo oxides. The crystallite size is less than approximately 20nm for the $Ni_{1+x}Fe_{2-x}O_4$ series and approximately 30nm or less for the $Ni_{1+y}Co_{2-y}O_4$ series. The crystallite size calculated from XRD analysis of $Ni_{1+x}Fe_{2-x}O_4$ and $Ni_{1+y}Co_{2-y}O_4$ nanoparticles is in good agreement with the previous literature.[8,11,17] Compositions of 33 mole-% Ni have the lowest crystallite size.

Raman spectra of nanoparticles synthesized by co-precipitation with different compositions of a) $Ni_{1+x}Fe_{2-x}O_4$ and b) $Ni_{1+y}Co_{2-y}O_4$ are presented in Figure 4. The $Ni_{1+x}Fe_{2-x}O_4$ spectra exhibit Raman modes at 690 cm^{-1} and 470 cm^{-1} while $Ni_{1+y}Co_{2-y}O_4$ nanoparticles have Raman modes at 467 and 672 cm^{-1}. These bands are consistent with the $Ni_{1+x}Fe_{2-x}O_4$ and $Ni_{1+y}Co_{2-y}O_4$ nanoparticles forming spinel structures of space group Fd-3m.[20] This space group results in

Table III. Crystallite diameter *d* of various compositions of $Ni_{1+x}Fe_{2-x}O_4$ and $Ni_{1+y}Co_{2-y}O_4$ nanoparticles synthesized by co-precipitation process. The diameters are given in nm as evaluated from the Scherrer Equation 5 applied to the peak with indices (*hkl*) as indicated in the table.

Ni/Fe or Ni/Co	mole-% Ni	NiFe *d*(311)	NiFe *d*(400)	NiCo *d*(222)	NiCo *d*(311)
0.1	9	21.3	18.5	-	-
0.33	25	17.2	16	-	-
0.5	33	14.05	10.9	-	-
0.75	43	16.1	13.2	-	-
0.1	9	-	-	33.1	29.5
0.33	25	-	-	22.28	21.8
0.5	33	-	-	12.3	16.2
0.75	43	-	-	13.7	16.7

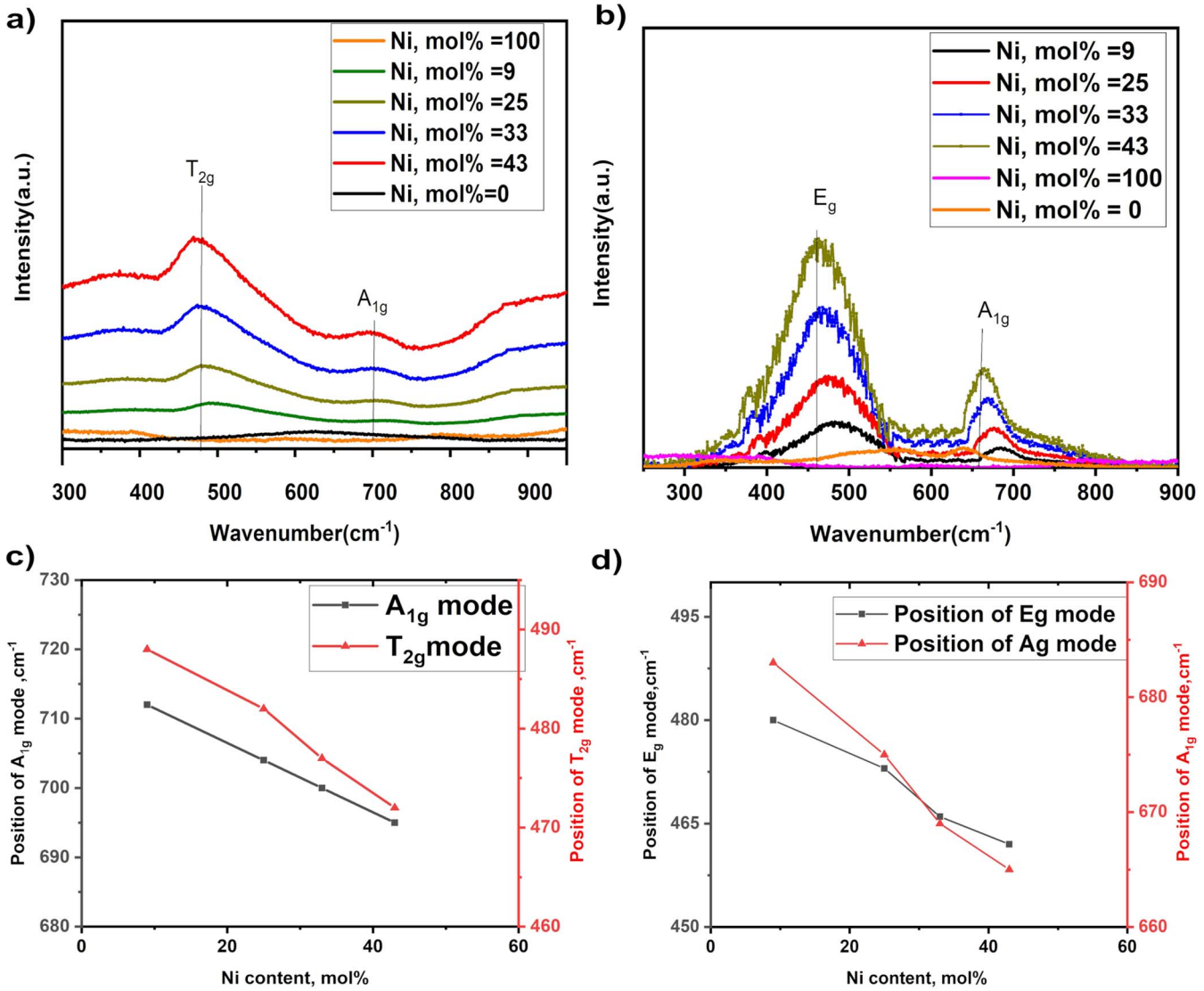

Figure 4. Raman Spectrum of a) $Ni_{1+x}Fe_{2-x}O_4$ and b) $Ni_{1+y}Co_{2-y}O_4$ nanoparticles of various mole-% Ni compositions prepared by co-precipitation, effect of composition on Raman peak shift of A_g and T_{2g} modes depending on x of c) $Ni_{1+x}Fe_{2-x}O_4$, and shift peak positions of A_g and E_g modes depending on x of d) $Ni_{1+y}Co_{2-y}O_4$.

five Raman active bands, namely $A_{1g} + E_g + 3T_{2g}$.[20,21] We assign the Raman modes at 690 cm^{-1} in the $Ni_{2+x}Fe_{2-x/2}O_4$ nanoparticles to the A_{1g} symmetry.[18,21] The mode T_{2g} at 470 cm^{-1} corresponds to the asymmetric stretching of oxygen vibrations of the octahedral group.[22,23] We assign the peaks at 467 and 672 cm^{-1} for $Ni_{1+y}Co_{2-y}O_4$ to the E_g and A_{1g} vibrational modes of $Ni_{1+y}Co_{2-y}O_4$, respectively. E_g and A_{1g} peaks are linked with Ni-O and Co-O vibration modes of the spinel $NiCo_2O_4$.[24]

The characteristic Raman peak positions as a function of composition are shown in Figure 4c for $Ni_{1+x}Fe_{2-x}O_4$ and in Figure 4d for $Ni_{1+y}Co_{2-y}O_4$. The Raman peak positions decrease almost linearly as the mole-% Ni increase. Such shifts are expected due to changes in mass and bond strengths with composition.[25]

Figure 5 shows the relationship between composition and BET surface area. The BET surface area of both the $Ni_{1+x}Fe_{2-x}O_4$ and $Ni_{1+y}Co_{2-y}O_4$ nanoparticles increases with increasing dopant concentration up to 33 mole-% Ni. Such increase in BET surface area has been related to crystal deformation caused by the dopant in the lattice of the host oxide.[26]

De Faria et al.[27] observed similar changes in the BET surface area with composition for Ni + Co oxides prepared by thermal decomposition of nitrates. In their case the BET surface area increased as Ni was added to Co_3O_4, or when Co was added to Ni oxides. The dependence of BET area on composition showed two maxima at 20 mole-% Ni and 90% in the oxides. Such behavior indicates a high degree of phase dispersion.[27] Whereas our series of investigations do not include any sample with composition close to 90% Ni, we do note that the maximum in Figure 5 here corresponds to 33 mole-% Ni, which is a little higher than the 20% found by De Faria et al.[27]

Figures 6a and 6b show measured zeta potentials as a function of pH for the $Ni_{1+x}Fe_{2-x}O_4$ and $Ni_{1+y}Co_{2-y}O_4$ series of catalysts, respectively. The pH at which the curves cross the abscissa vary systematically with composition and therefore imply a correspondingly systematic variation in the isoelectric point (IEP) with composition. This is shown explicitly in Figures 4c and 4d, which show the isoelectric potentials (IEPs) for $Ni_{1+x}Fe_{2-x}O_4$ and $Ni_{1+y}Co_{2-y}O_4$, respectively, as a function of composition. For the Ni-Fe catalyst the IEP increase from that of Fe_3O_4, reaches a plateau, and then increases again toward the value for NiO. For the Co-containing catalyst the IEP increases from its value for Co_3O_4 and displays a maximum at 33 mole-% of Ni after which it decreases slightly. Thus, neither catalyst would appear to conform to Park's law[28] if the surface composition is assumed to be identical to the bulk composition.

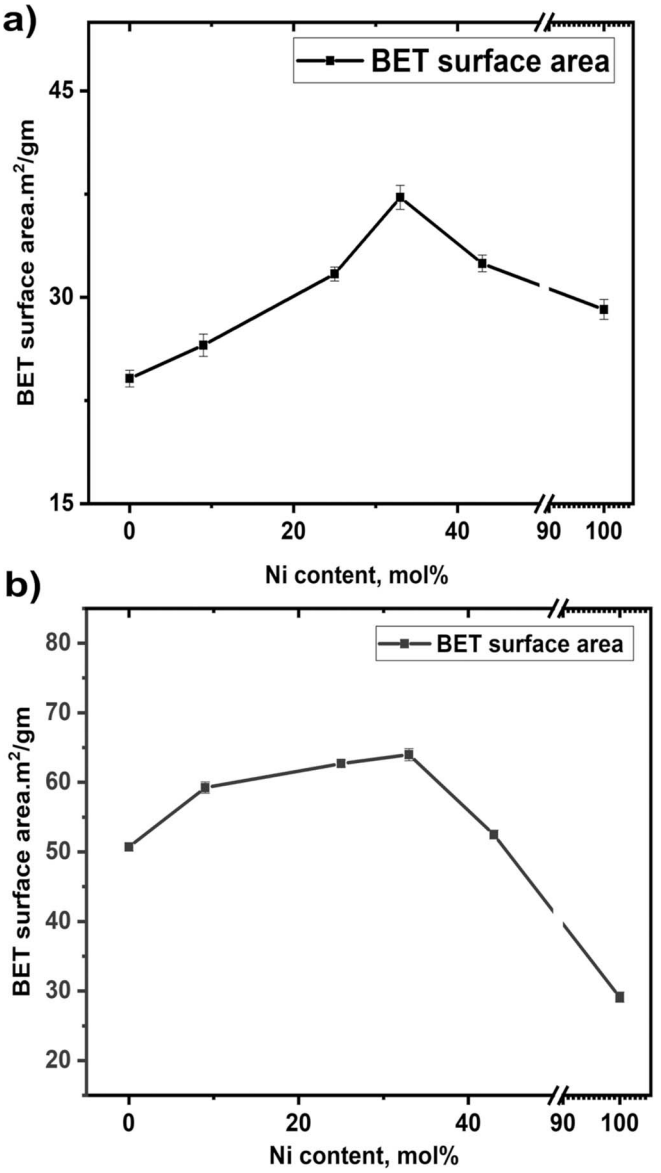

Figure 5. BET surface area of a) $Ni_{1+x}Fe_{2-x}O_4$ and b) $Ni_{1+y}Co_{2-y}O_4$ nanoparticles of different mole-% Ni compositions prepared by the co-precipitation process.

The IEP values for Co_3O_4 (7.5), Fe_3O_4 (6.6), $NiCo_2O_4$ (9.1), $NiFe_2O_4$ (7.6), and NiO (8.8) are consistent with previously reported values from the literature.[29–31]

We expect the IEP to primarily reflect the surface of the catalysts and to be less sensitive to bulk composition. De Faria et al.[27] showed that for NiCo oxides the point of zero charge (pzc) correlates with surface segregation of Ni in the oxides, as assessed by XPS.[27] In the absence of specific adsorption the pzc and the IEP will coincide.[30] We therefore take the IEP for our $Ni_{1+y}Co_{2-y}O_4$ catalysts to reflect strong surface segregation[27,32] also in our case. The zeta potential measurements therefore indicate that the $Ni_{1+x}Fe_{2-x}O_4$ surface is strongly enriched in Ni, and for intermediate composition independent on nominal composition.

The results are similar for $Ni_{1+x}Fe_{2-x}O_4$, but in this case the plateau at intermediate composition is lower than that corresponding to pure NiO. Therefore, it appears that in this case the surface composition is also approximately independent of nominal composition, but with a lower Ni content than that corresponding to a pure Ni catalyst.

Based on structural and composition investigation, $NiFe_2O_4$ and $NiCo_2O_4$ will represent NiCo and NiFe oxides with 33 mole-% Ni respectively in all results.

Electrocatalytic activity and kinetics analysis.—The electrochemical performance of the various $Ni_{1+x}Fe_{2-x}O_4$ and $Ni_{1+y}Co_{2-y}O_4$ catalysts is shown in Figure 7, which shows current vs. potential during an LSV performed in an N_2-saturated 0.1 mol dm^{-3} at an electrode rotating at 1600 rpm. Figures 7a and 7b show the LSV curves normalized with respect to the geometric surface area of the electrode. All data presented in Figure 7 were obtained after the electrode had been subjected to cathodic activation through ten consecutive LSVs, which ensured stable performance of the electrodes.

As can be observed in Figure 7 with the catalysts with 33 mole-% Ni ($NiFe_2O_4$) and ($NiCo_2O_4$) have the lowest onset potentials for the HER in 0.1 mol dm^{-3} KOH, approximately −200 mV for both catalysts. The corresponding onset potentials for Fe_3O_4 and NiO are −400 mV and −280 mV, respectively. We have taken the onset potential from Figure 7 as the potential at which the absolute value of the current normalized to geometric area has risen 5% above the double layer current. The onset potentials for the nanoparticle catalysts are thus very much smaller than those observed for Vulcan XC/72 (−1.01 V) and a bare GC electrode (−1.1 V).[33]

As shown in Figure 7 $NiCo_2O_4$ represents the highest electroactivity toward HER and requires an overpotential of −317 mV at −10 mA cm^{-2}. With $NiFe_2O_4$ −10 mA cm^{-2} is achieved at an overpotential of −330 mV in 0.1 mol dm^{-3} KOH, which therefore has higher HER activity than the $NiFe_2O_4$ nanoparticles with mass loading (2.2 mg cm^{-2}) reported by Kumar et al.[33]

To separate intrinsic electrocatalytic activity from effects of surface we explore several methods for area normalization below. We thus normalize with respect to the BET surface area, the surface area evaluated from the voltammetric charge, and the surface area evaluated from the double layer capacitance for the $Ni_{1+x}Fe_{2-x}O_4$ samples and the $Ni_{1+y}Co_{2-y}O_4$ samples, respectively. We will refer to the two latter as the voltammetric electrochemical surface area (VECSA) and the double-layer electrochemical surface area (DECSA), respectively. The surface area evaluated from the voltammetric charge (VECSA, $S_{\alpha-Ni(OH)_2}$) is based on the equation[34]

$$S_{\alpha-Ni(OH)_2} = \frac{Q_{CV}}{514\ \mu C\ cm^{-2}} \quad [6]$$

where Q_{CV} (in $\mu C\ cm^{-2}$) is the anodic voltammetric charge evaluated in 0.1 mol dm^{-3} by integration from −0.9 V through −0.4 V vs Hg/HgO. Prior to the voltammetry the electrodes were polarized at $E = -1.3$ V vs. Hg/HgO for 5 minutes and then at $E = -0.8$ V vs. Hg/HgO for 10 min to reduce and eliminate any surface oxides/hydroxides traces.[14,34]

The charge in the denominator, 514 $\mu C\ cm^{-2}$, is the charge corresponding to formation of α-$Ni(OH)_2$ monolayer from Ni.

$$Ni(s) + 2OH^-(aq) \rightarrow \alpha\text{-}Ni(OH)_2(s) + 2e^- \quad [7]$$

The DECSAs of the catalyst samples were calculated from the double layer capacitance according to Eq. 8.[23] The DECSA (S_{dl}) was thus determined from the double layer capacitance C_{dl} through

$$S_{dl} = \frac{C_{dl}}{C_s} \quad [8]$$

The double layer capacitance C_{dl} was calculated from the slope of plots of current vs. sweep rate in the double-layer region in which there were no signs of faradaic reaction as inferred from the current being independent of the electrode potential. C_s is the specific capacitance of the sample and corresponds (ideally) to the capacitance of an atomically smooth planar surface of the material per unit area under identical electrolyte conditions. For our estimates here we used the value $C_s = 0.04$ mF cm^{-2} in Eq. 8. This is based on typical values for C_s for solutions of 0.1 mol dm^{-3} KOH[35,36] in which our measurements were performed.[37] Also, for the double-layer capacitance

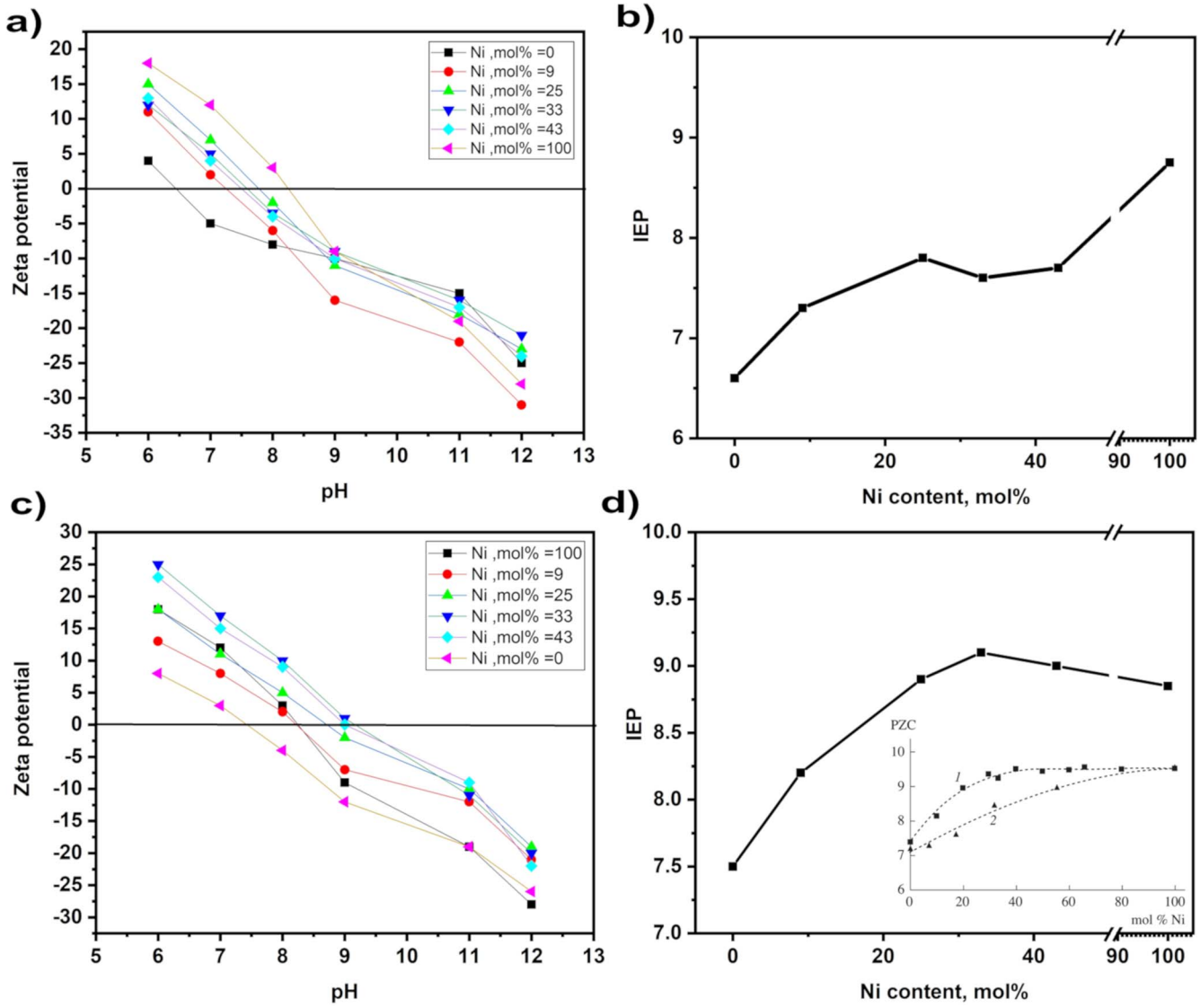

Figure 6. Titration curves for zeta potential vs pH for various a) $Ni_{1+x}Fe_{2-x}O_4$ and c) $Ni_{1+y}Co_{2-y}O_4$ nanoparticle with various Ni mole-% compositions, and isoelectric point as a function of b) $Ni_{1+x}Fe_{2-x}O_4$ and d) $Ni_{1+y}Co_{2-y}O_4$ nanoparticles composition. Onset in Figure 6d : pzc dependence on nominal mixed oxides composition of NiO + Co_3O_4 : (1) chemical and (2) physical mixtures. Data from Figure 12 in E. Guerrini and S. Trasatti, *Russ. J. Electrochemistry*, **42** 1017 (2006).

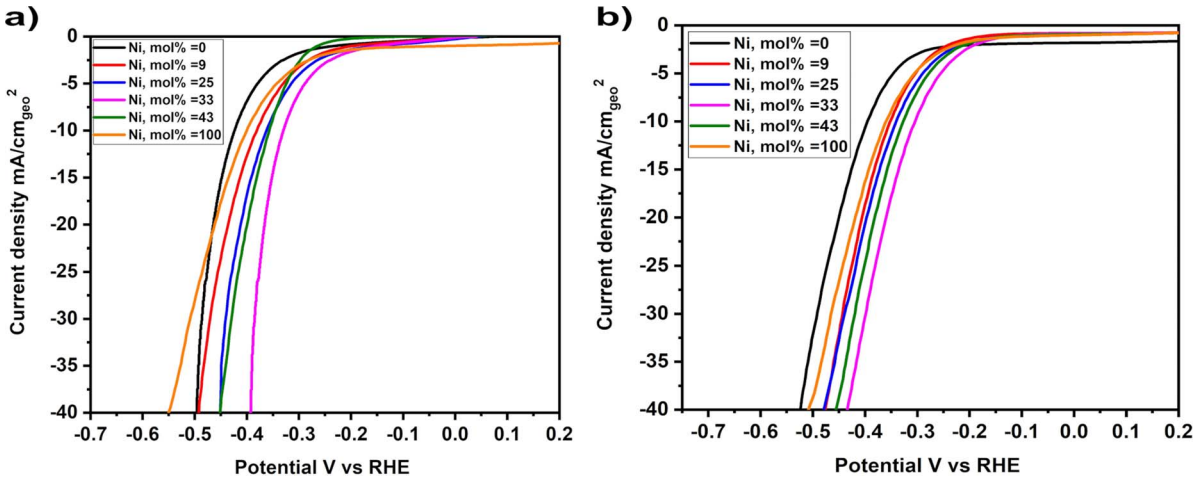

Figure 7. Linear sweep voltammetry (LSV) for HER normalized to the geometric surface area of a) $Ni_{1+x}Fe_{2-x}O_4$ and b) $Ni_{1+y}Co_{2-y}O_4$ nanoparticle compositions respectively, data obtained in N_2-saturated 0.1 mol dm^{-3} KOH with a rotation rate of 1600 rpm using Nafion as a binder.

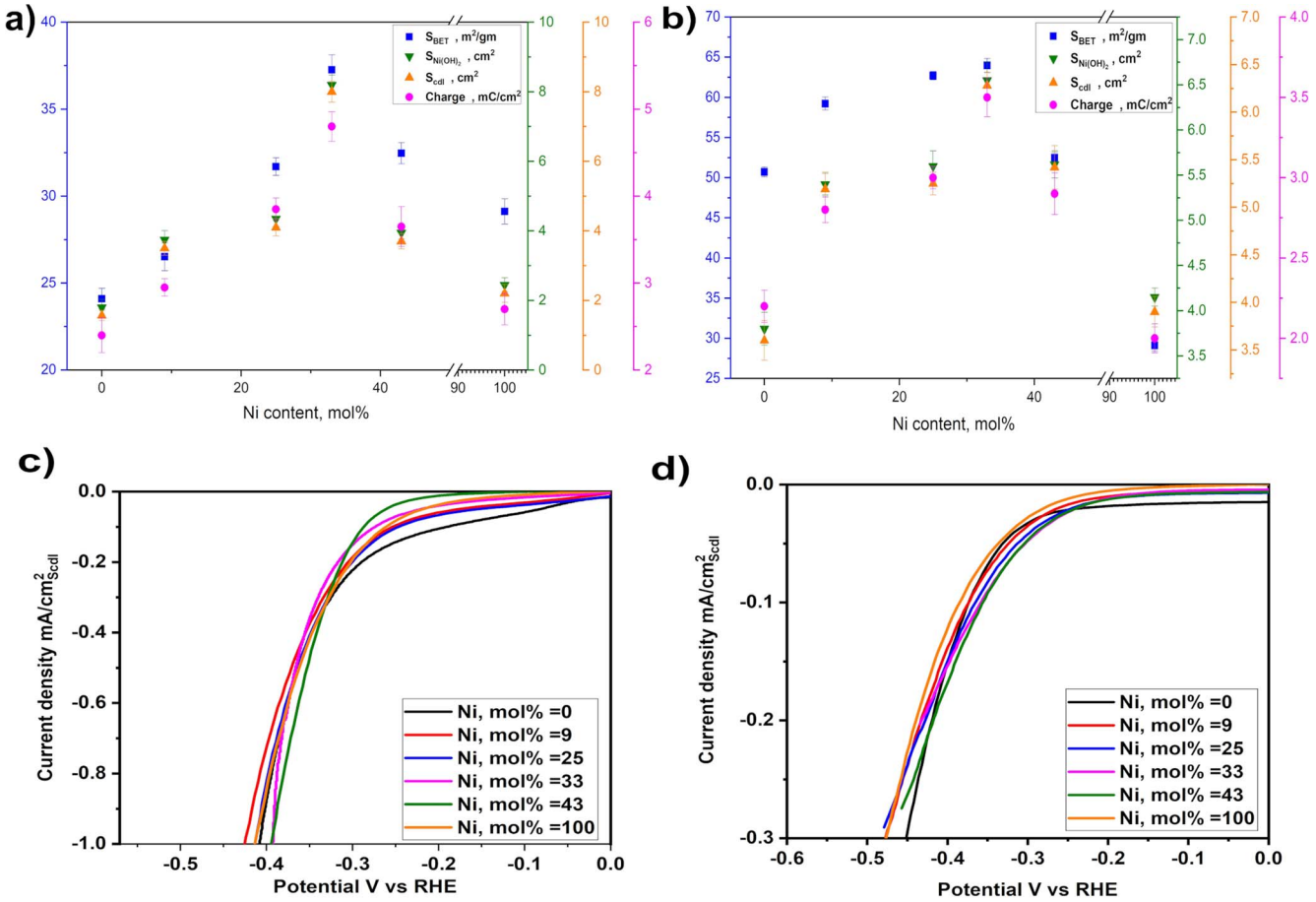

Figure 8. Charge and Specific surface area of a) $Ni_{1+x}Fe_{2-x}O_4$ and b) $Ni_{1+y}Co_{2-y}O_4$, derived from BET, $Ni(OH)_2$ charge and double layer capacitance, while c) $Ni_{1+x}Fe_{2-x}O_4$ and d) $Ni_{1+y}Co_{2-y}O_4$ represent current normalized to S_{dl} for different compositions.

measurements we have assumed that the metal oxide catalysts are equally conductive.[38]

The average BET, VECSA, and DECSA values for each catalyst as function of composition is displayed in Figure 8. The two electrochemical surface areas, i.e. the VECSA and the DECSA are in very good agreement, but the BET gives much larger values than these for all compositions. The qualitative trend is the same for all three, however, showing a distinct maximum and, with the exception of the BET area for the $Ni_{1+y}Co_{2-y}O_4$ at low Co content, a fairly symmetric curve about this maximum. The surface areas for the two end members are reasonably similar.

Normalizing the currents of the different $Ni_{1+x}Fe_{2-x}O_4$ and $Ni_{1+y}Co_{2-y}O_4$ catalysts with respect to the DECSA (S_{dl}) results in almost overlapping curves, as shown in Figures 8c and 8d. Figure 8 thus appears to indicate that the intrinsic catalytic activity of the catalysts is the same and independent of surface area.[14,39]

The results in Figure 8 thus indicates that the DECSA-normalized activity and thus the surface-area specific catalytic activity is the same and independent of composition for all catalysts. Changing the composition of $Ni_{1+x}Fe_{2-x}O_4$ and $Ni_{1+y}Co_{2-y}O_4$ catalysts prepared by co-precipitation thus modifies the catalytic activity of the catalysts primarily through a modification of the electroactive surface area.[27,32,40] Lower crystallite size and higher electrochemical surface area lead to higher apparent HER activity at 33 mole-% Ni.[27,32,40]

Tafel plots (the overpotential η vs. the logarithm of (absolute value of the) current density $|i|$) are shown in Figures 9a and 9c. The linear regions of the Tafel plots were fitted to the Tafel equation,

$$\eta = a + b \log i \qquad [9]$$

where b is Tafel slope[41] and a is a constant.

All the catalysts, both those from the $Ni_{1+x}Fe_{2-x}O_4$ series and those of the $Ni_{1+y}Co_{2-y}O_4$ series, have similar Tafel slopes. These are close to 120 mV/dec. Figure 9 also shows Tafel impedances as extracted from electrochemical impedance spectroscopy (EIS) measurements at an overpotential of −200 mV. The Tafel impedance is defined as[42,43]

$$Z_t = \left(\frac{\hat{E}}{\hat{i}}\right) i_{st} \qquad [10]$$

where i_{st} ia the steady-state current density at which the impedance was recorded, and $\hat{E}$ and $\hat{i}$ are the complex amplitudes of potential and current.

The solution resistance as determined from the high-frequency intercept of the impedance-plane plot with the real axis was subtracted from all data. From the Tafel impedance the Tafel slope may be found from the radius of the arc in the impedance-plane plot. (For an example of such an analysis, see Ref. 42). The Tafel impedances in Figures 9c and 9d appear to cluster around 150 mV/dec, in reasonable agreement with the Tafel plots.

Figure 9, Tables IV and V display in detail the good agreement between the semi steady state polarization Tafel and Tafel impedance plots.

Figures 10a and 10b display polarization curves for $NiFe_2O_4$ and $NiCo_2O_4$ compositions at different pH from 11 to 14. The polarization curves are clearly dependent on the solution pH, and the current consistently increases with decreasing pH at constant potential. For pH 14, the curve was extrapolated to potentials below the Tafel region in order to provide the currents at this pH for the same potential as for the data for higher pH. From these curves we evaluated the reaction orders from the slope Ω in plots of current density vs. pH at constant

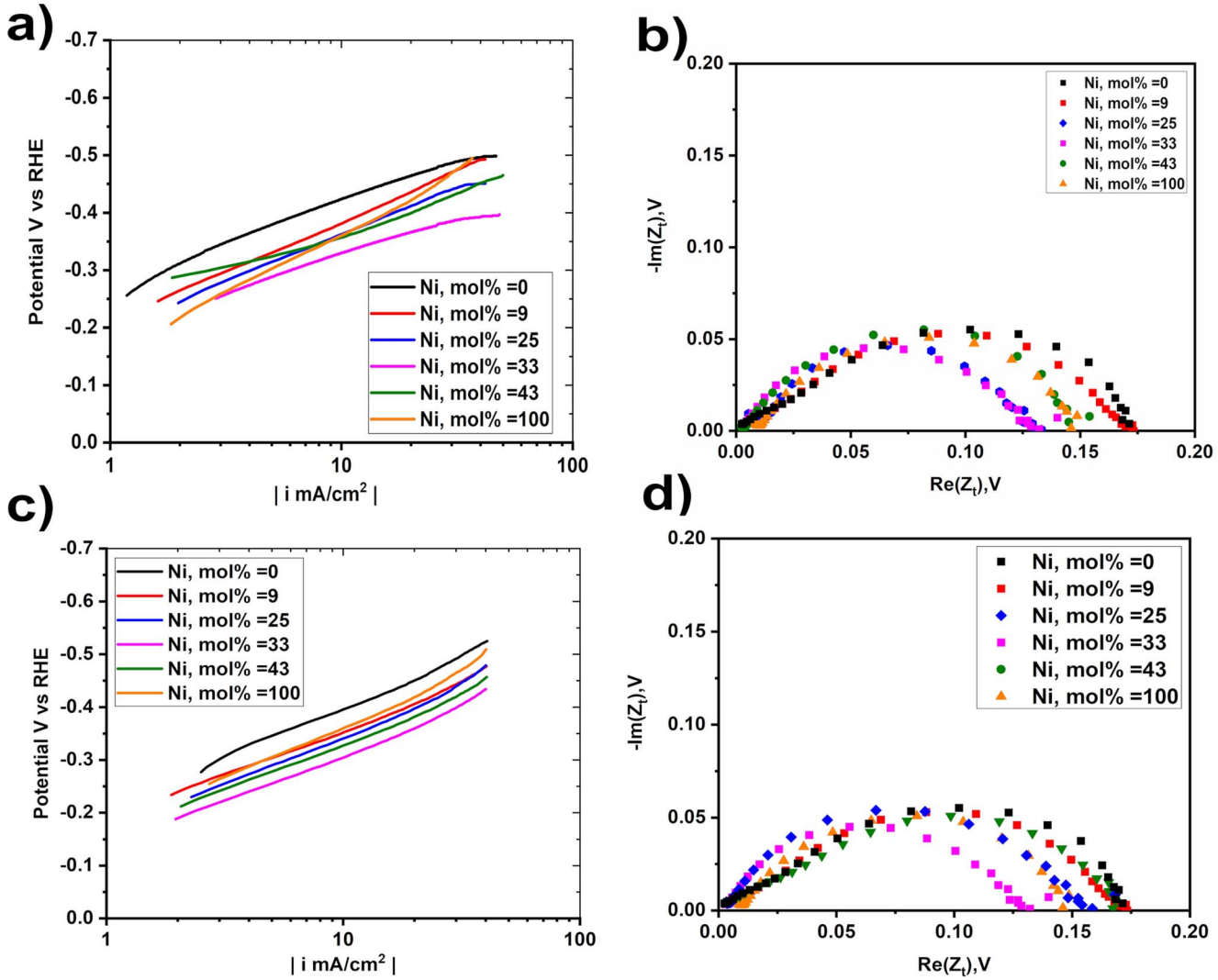

Figure 9. Tafel plot resulted from LSV measurements for a) $Ni_{1+x}Fe_{2-x}O_4$ and c) $Ni_{1+y}Co_{2-y}O_4$ various nanoparticle compositions, Tafel impedance of b) $Ni_{1+x}Fe_{2-x}O_4$ and d) $Ni_{1+y}Co_{2-y}O_4$ nanoparticles at overpotential −200 mV, obtained in N_2-saturated 0.1 mol dm^{-3} KOH with a rotation rate of 1600 rpm.

Table IV. The values of Tafel slope and corresponding charge transfer coefficient, produced from semi steady state polarization and Tafel impedance of different $Ni_{1+x}Fe_{2-x}O_4$ compositions (with an accuracy of ± 5 mV/decade and ± 0.04 respectively).

Ni/Fe	mole-% Ni	Polarization Tafel slope (charge transfer coefficient)	Tafel impedance (charge transfer coefficient)
0	0	188 (0.31)	172 (0.34)
0.1	9	175 (0.33)	175 (0.33)
0.33	25	155 (0.37)	138 (0.42)
0.50	33	130 (0.45)	132 (0.44)
0.75	43	160 (0.36)	143 (0.41)
∞	100	169 (0.35)	148 (0.39)

Table V. The values of Tafel slope and corresponding charge transfecoefficient, produced from semi steady state polarization and Tafel impedance of different $Ni_{1+y}Co_{2-y}O_4$ compositions (with an accuracy of ± 5 mV/decade and ± 0.04 respectively).

Ni/Co	mole-% Ni	Polarization Tafel slope, mV/dec (charge transfer coefficient)	Tafel impedance, mV (charge transfer coefficient)
0	0	180 (0.33)	171 (0.34)
0.1	9	185 (0.32)	174 (0.34)
0.33	25	170 (0.34)	161 (0.36)
0.50	33	125 (0.47)	130 (0.45)
0.75	43	178 (0.33)	165 (0.35)
∞	100	165 (0.35)	150 (0.39)

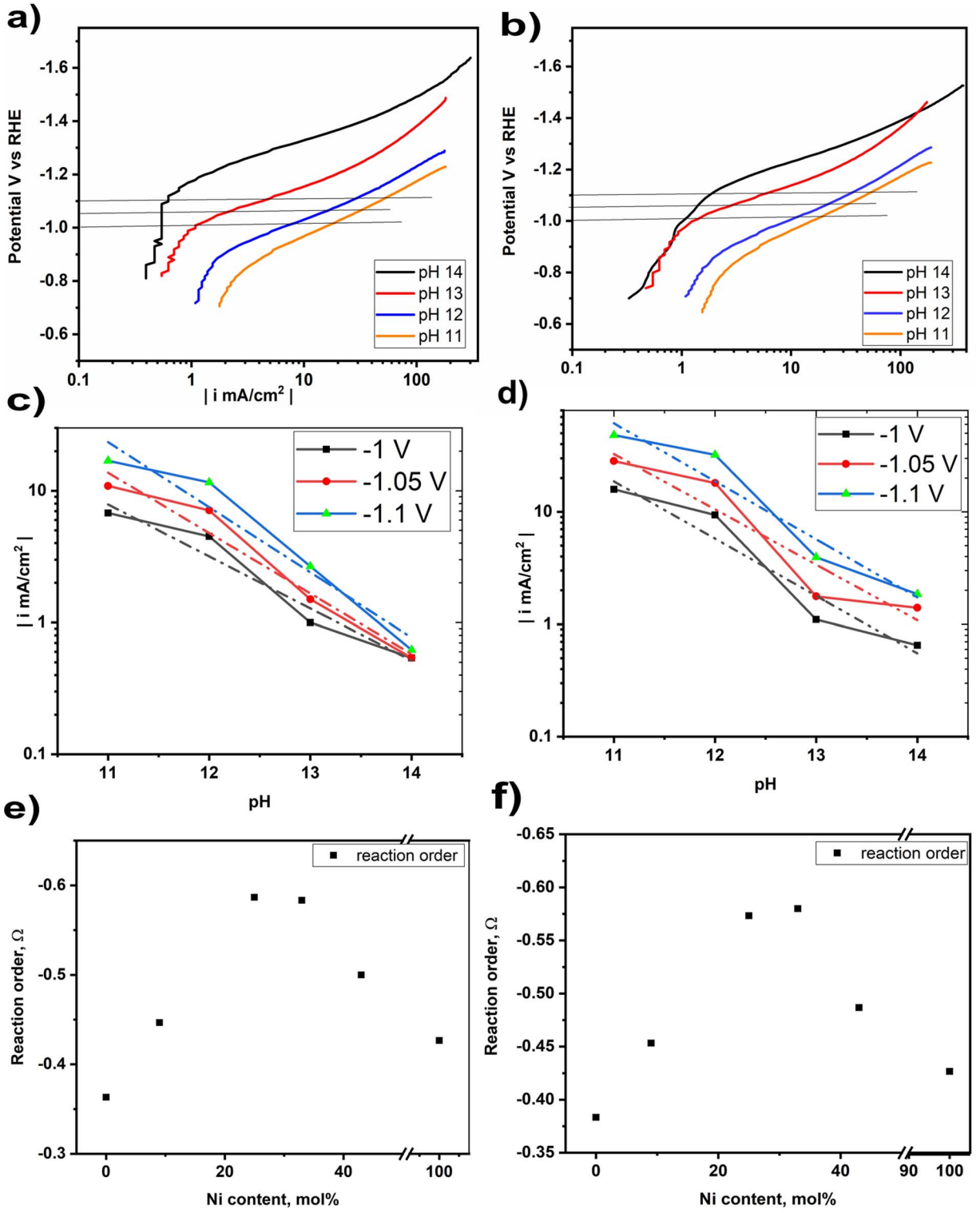

Figure 10. Polarization curves of a) $NiFe_2O_4$ and b) $NiCo_2O_4$ at pH 14, 13, 12 and 11. Reaction order plots of c) $NiFe_2O_4$ and d) $NiCo_2O_4$. Reaction order - composition relationship of e) $Ni_{1+x}Fe_{2-x}O_4$ and f) $Ni_{1+y}Co_{2-y}O_4$, data obtained with a rotation rate of 1600 rpm.

potential. The resulting plots are shown in Figures 10c and 10d for potentials of −1, −1.05, and −1.1 V vs Hg/HgO for $NiFe_2O_4$ and $NiCo_2O_4$ compositions and NiO.

Figures 10e and 10f displays the resulting reaction order as a function of composition of $Ni_{1+x}Fe_{2-x}O_4$ and $Ni_{1+y}Co_{2-y}O_4$ and NiO nanoparticles. For $Ni_{1+x}Fe_{2-x}O_4$ and $Ni_{1+y}Co_{2-y}O_4$ nanoparticles the reaction orders were found to decrease from −0.36 for Fe_3O_4 and −0.4 for Co_3O_4 to −0.585 for $Ni_{0.74}Fe_{2.26}O_4$ and −0.578 for $NiCo_2O_4$. For higher Ni-content it increases to −0.42 for NiO. The reaction order is thus not integer.

Tafel slopes and reaction orders reflect the inherent catalytic properties of the HER catalysts. An indication of the reaction mechanism of the HER and the rate-determining step (RDS) can be obtained from an analysis of these. The overall reaction may proceed through two pos-

sible reaction pathways: Volmer– Heyrovsky and Volmer– Tafel.[7] We therfore consider the following reaction mechanisms for the HER,[40,44]

$$S + H_2O(\ell) + e^- \underset{k_{-11}}{\overset{k_{11}}{\rightleftharpoons}} S{-}H + OH^-(aq) \quad [11]$$

$$S{-}H + H_2O(\ell) + e^- \underset{k_{-12}}{\overset{k_{12}}{\rightleftharpoons}} S + OH^-(aq) + H_2(aq) \quad [12]$$

$$S{-}H + S{-}H \underset{k_{-13}}{\overset{k_{13}}{\rightleftharpoons}} S + H_2(aq) \quad [13]$$

where S represents a surface site (NiO, FeO, or CoO or the corresponding metal atoms in oxidation state zero). The Volmer reaction, Eq. 11, involves electroreduction of water molecules with hydrogen adsorption, the Heyrovsky reaction, Eq. 12, involves electrochemical hydrogen desorption, and the Tafel reaction, Eq. 13, involves chemical desorption.[41,46]

The rate constants in Eqs. 11 and 12 are potential dependent and take the form

$$k_{11} = k_{11}^0 \exp\left\{\frac{-\alpha FE}{RT}\right\} \quad [14]$$

$$k_{-11} = k_{-11}^0 \exp\left\{\frac{(1-\alpha)FE}{RT}\right\} \quad [15]$$

$$k_{12} = k_{12}^0 \exp\left\{\frac{-\alpha FE}{RT}\right\} \quad [16]$$

$$k_{-12} = k_{-12}^0 \exp\left\{\frac{(1-\alpha)FE}{RT}\right\} \quad [17]$$

where the pre-exponentials k_{11}^0, k_{-11}^0, k_{12}^0 and k_{-12}^0 are all potential independent. In principle the charge-transfer coefficient α may be different for the two electrochemical steps, but our data do not allow for any distinction between them and we will therefore not make it. The rate constants for Reaction 13 we will take as potential independent. In these equations R is the gas constant, T the temperature, F the Faraday constant, α a charge-transfer coefficient (or symmetry factor), and E the electrode potential.

If Reaction 11 is the *rds* the Tafel slope is trivially equal to $b = -RT/\alpha F$ (or $b = -\ln 10 RT/\alpha F = -2.303RT/\alpha F$ for a base-10 logarithm) and the reaction order with respect to OH^-, Ω_{OH^-}, is $\Omega_{OH^-} = 0$ at all (negative) values of E.[41,46] With $\alpha = 0.5$ this would give a Tafel slope of 118 mV at room 298 K. The current is, according to this mechanism and and *rds*, independent of pH.

If Reaction 12 is *rds* the current will be given by

$$i = -2F\Gamma k_{12}^0 \theta_H \exp\left(\frac{-\alpha FE}{RT}\right) \quad [18]$$

where i is the current density, θ_H is the coverage of adsorbed hydrogen, and Γ is the number of moles of adsorbed hydrogen per surface area at $\theta_H = 1$. The other symbols take the same meaning as above. Setting the forward rate of reaction Eq. 11 equal to its backward rate and insertion into Eq. 18 gives (see also Appendix A)

$$i = -\frac{2F\Gamma k_{12}^0 \exp(-\alpha FE/RT)}{1 + K_{-11}\left[OH^-\right]\exp(FE/RT)} \quad [19]$$

which predicts a Tafel slope and reaction order equal to $b = -RT/(1+\alpha)F$ (or $b = -2.303RT/(1+\alpha)F$ for a base-10 logarithm) and $\Omega_{OH^-} = -1$ at small negative values of E and $b = -RT/\alpha F$ and $\Omega_{OH^-} = 0$ large and negative E, consistent with Eq. 20 below. With $\alpha = 0.5$ this would give Tafel slopes of 39 mV at small (and negative) potential and 118 mV at large (and negative) potential. A derivation similar to that in Reference 47 gives explicit relation between the Tafel slope and the reaction order,

$$b^{-1} = \frac{F}{RT}(-\alpha + \Omega_{OH^-}) \quad [20]$$

which corresponds to a similar equation derived by Tilak and Conway[47] for acid conditions.

If Reaction 13 is *rds* the current is determined by

$$i = -2F\Gamma k_{13}\theta_H^2 \quad [21]$$

and insertion of Eq. A2 from Appendix A gives

$$i = -2F\Gamma k_{13}^0 \left[\frac{1}{1 + K_{-11}\left[OH^-\right]\exp(FE/RT)}\right]^2 \quad [22]$$

which predicts a Tafel slope of −30 mV at small and negative E and a limiting current at large and negative E. The reaction order with respect to hydroxyl ions is −2 and 0 for these two cases, respectively. A derivation along the lines leading to Eq. 20 gives $b^{-1} = (F/RT)\,\Omega_{OH^-}$.

The Tafel slope of 120 mV therefore suggests that the Volmer step, Eq. 11, is rate-determining. On the other hand, the fractional reaction orders are not consistent with this conclusion.

The observed fractional reaction order for the catalysts studied here can, however, be understood in terms of surface acid-base equilibria between the catalyst surface and the solution.[40,48,49] A derivation for the case that Reaction 11 is the *rds* is reproduced in Appendix B and gives the relation

$$\Omega = \left.\frac{\partial \log|i|}{\partial(\mathrm{pH})}\right|_{E,T} = -\alpha \quad [23]$$

and predicts that the slope of the current vs. pH will be equal to the negative of the charge-transfer α. Since $0 < \alpha < 1$ and we expect its value to be in the order of 0.5. The result in Figure 10, in which α ranges from 0.4 through 0.6, are therefore quite reasonable. Similar observations with fractional reaction order have been made for other electrocatalysts for both the hydrogen evolution reaction[14,40,50,51] and the oxygen evolution reaction.[48,49,52–54]

The experimental values of Tafel slope in Tables IV and V range from 125 to 188 mV/dec, indicating that the Volmer reaction is the rate-determining step for the HER on all oxide electrodes investigated. $NiFe_2O_4$ and $NiCo_2O_4$ show a Tafel slope of 130 and 125 mV /dec respectively which is relatively small compared to those of the other $Ni_{1+x}Fe_{2-x}O_4$ and $Ni_{1+y}Co_{2-y}O_4$ compositions. A lower Tafel slope implies a higher change in the hydrogen production rate for a given change in overpotential. If Eq. 11 is rate-determining the charge transfer coefficient, α, can be calculated from the Tafel slope b[55]

$$\alpha = \frac{2.303RT}{bF} \quad [24]$$

The results are given in Tables IV and V. $NiFe_2O_4$ and $NiCo_2O_4$ show average transfer coefficients value that are higher than that of the other $Ni_{1+x}Fe_{2-x}O_4$ and $Ni_{1+y}Co_{2-y}O_4$ compositions.

The Tafel slopes obtained here are similar to those found for Ni metal, in line with studies by Oshchepkov et al.,[44] and the oxidation state does not appear to have a significant effect on Tafel slopes for Ni compounds in these cases. The Tafel slopes for Ni metal range from 115 to 129 mV/decade while the Tafel slopes of oxidized Ni are in the range of 125–130 mV/dec for the HER.[44] This may be related to similarities in the state of surface Ni in the oxides and metal when exposed to the ambient air or water. When a Ni surface is exposed to air or aqueous solution, atomic layers comprised of two distinct layers forms: a $Ni(OH)_2$ layer at the air-oxide interface and NiO layer between the metal substrate and the outer hydroxide layer. A thin hydroxide film forms when a NiO surface exposed to the atmosphere or an aqueous solution. Ni or NiO transformation to $Ni(OH)_2$ could be accelerated in alkaline condition.[56]

On the other hand, at the low potentials of the HER the surface atoms may be reduced to the metallic state. Density functional theory (DFT) calculations by Dong et al.[45] show that at metallic Ni(111) surfaces, i.e. with Ni in oxidation state zero, the surface binds hydrogen atoms too tightly for maximum reaction rate. At oxidized Ni atoms the binding energy of hydrogen becomes even stronger. However, at Ni atoms in oxidation state zero in the vicinity of oxidized Ni

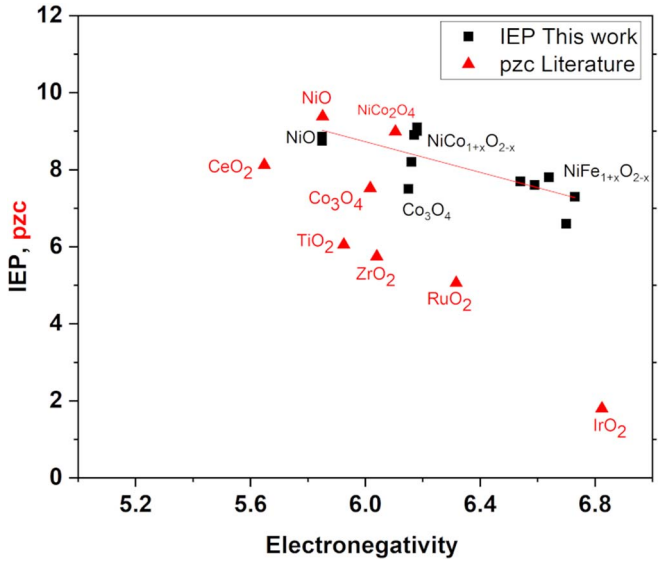

Figure 11. IEP of Oxides plotted vs. oxide electronegativity for $Ni_{1+x}Fe_{2-x}O_4$ and $Ni_{1+y}Co_{2-y}O_4$ catalyst nanoparticles from this work and compared to literature values.[69]

the adsorption energy for hydrogen decreases, and catalytic activity increases. The high surface activity observed here may indicate that the surface is not fully oxidized and that there is such an interaction between odixized and metallic metal sites also in our catalysts.

Assuming therefore that the electrocatalytic properties of Ni, Co, and Fe in our oxides parallel the electrocatalytic properties of the metal, the proximity of these metals usually found in volcano plots[57,58] indicate that one should also expect similar catalytic properties of the three oxides, in line with our findings.

The catalytic activity for the HER of the oxides investigated here can also be rationalized based on the IEP. Trasatti has suggested the pzc as a descriptor for oxide catalytic activity.[59,60] The pzc will be determined by the acid-base properties of the surface, and therefore reflects the electronegativity of the oxide. Butler and Ginley[61] thus correlated the pzc of oxides with their electronegativity. We expect the electronegativity, in turn, to reflect the binding energy of adsorbates to the surface in general, and therefore also the electrocatalytic activity of that surface.

The results above that all the different oxides have similar electrocatalytic activities can therefore be rationalized in terms of their similar IEP values. The IEP measured here is expected to be similar to the pzc. Therefore the IEP should be correlated to the electronegativity of the oxides and thus to the binding energy of adsorbates. By calculating electronegativity of oxides (M_aO_b) defined as

$$\chi_{ox} = (\chi_M^a \chi_O^b)^{1/(a+b)} \quad [25]$$

a direct relation between IEP and electronegativity can be obtained,[31,61]

$$IEP = 20.66 - [1.98\,(\chi_{ox})] \quad [26]$$

From Figure 11, electronegativities of all our oxides cluster around 6, and hence we expect the bond energy to be nearly the same. This explains the comparable intrinsic activity of these oxides. Based on these results we proposed that reported NiCo and NiFe catalysts activities are not intrinsic but rather due to catalyst surface area as a result of the synthesis process. Similar results for NiMo were recently reported by Schalenbach et al.[62]

Catalyst ionomer interaction.—The ionomer acts as a stabilizing and binding agent in catalyst-solvent inks. Ionomers are used as binders to assist industrial water electrolysis applications, where an ionomer is essential to exchange either protons or hydroxide ions between anode and cathode. Nafion is the most regularly used binder in RDE screening of electrocatalysts for HER.

Although Nafion is a proton conducting polymer, it is commonly used also for HER screening in alkaline electrolytes. This has the drawback that the results obtained cannot be used directly for assessment of the performance of a catalyst in a membrane electrode assembly (MEA). This is because an anion-exchange membrane, in which hydroxide ions are transferred, is required in alkaline water electrolysis MEAS,[63] at least if the unit is fed with pure water or the electrolyte has a low concentration of hydroxyl ions. For these reasons, we studied the effect of ionomer by comparing the performance of Nafion with the anion-exchange ionomer (Fumion FAA-3).

Figure 12 demonstrates the effect of ink binder on electrochemical activity of $NiFe_2O_4$ and $NiCo_2O_4$. The influence of binder was assessed using Nafion and Fumatech ionomers. The HER activity changes significantly if Nafion is used instead of the Fumion FAA-3 ionomer. The highest value is observed with Nafion, which gives -10 mA cm^{-2} at overpotentials -330 and -317 mV for $NiFe_2O_4$ and $NiCo_2O_4$, respectively. With the Fumion FAA-3 ionomer we achieved a current density -10 mA cm^{-2} at overpotentials -350 and -360 mV for $NiFe_2O_4$ and $NiCo_2O_4$, respectively, as shown in Figure 12.

The difference in activity when using acidic and anion exchange ionomer can be rationalized considering factors such as the nature of the ionomer backbone and the affinity for water. The ionomer backbone is positively charged in Fumion FAA-3 and negatively charged in Nafion.[63] Also, the quaternary ammonium (QM^+) moiety may apply an electrostatic influence, reducing the catalyst HER activity as explained by Bates et al.[13] Nafion also has a higher affinity for water than the Fumion ionomer as indicated by the measured values of water uptake (37 wt% for Nafion vs. 26 wt% for Fumion FAA-3), may result in a higher kinetic current density in the RDE tests.[63] Overall, our results indicate that the ionomer does not only play a role as a binder but also influences the electrocatalyst activity for HER.

HER stability and durability.—Figure 13 displays Bode plots of $NiFe_2O_4$ and $NiCo_2O_4$ at different applied potentials (-150 to -300 mV vs. RHE) in 0.1 mol dm^{-3} KOH using Nafion binder. For all investigated overpotentials, the Bode plot shows a one time constant process in both $NiFe_2O_4$ and $NiCo_2O_4$. The solution resistance controls the impedance at high frequencies, and the Bode plot display zero slope at 0° phase angle. A linear dependence of the modulus of the impedance $|Z|$ vs. logarithm of frequency and a pronounced maximum in θ are features consistent with capacitive behavior at intermediate frequencies.

The impedance plateaus equal the sum of solution and charge transfer resistances in the low-frequency region.[64] The Bode diagram indicates that the value of the maximum phase angle decreases and the frequency at the maximum shifts to higher values at higher applied potentials.[64,65]

At higher applied potential, $NiFe_2O_4$ and $NiCo_2O_4$ have a lower charge transfer resistance (R_{ct}) and hence a higher rate of hydrogen evolution.[64,65] The impedance data were simulated using a modified Randles circuit involving solution resistance (R_s) in series with the charge transfer resistance (R_{ct}) of the HER, which is in parallel with a constant phase element (CPE). The same circuit is used to model EIS data obtained for Ni HER in alkaline solutions by several research groups.[66]

Figure 14 shows chronoamperometry results of $NiFe_2O_4$ and $NiCo_2O_4$ at an applied potential of -350m V for 24 hours in 0.1 mol dm^{-3} KOH using Nafion binder. $NiFe_2O_4$ and $NiCo_2O_4$ were chosen for durability measurements as they possess the highest electrochemical activity. The constant current with time displayed in the figure indicates that $NiFe_2O_4$ and $NiCo_2O_4$ exhibit a good stability during hydrogen evolution in alkaline media.[67]

Stability is essential for practical applications of a catalyst. The cost of hydrogen production is directly related to the lifetime of the catalyst. Our short-term measurements indicate these highly active catalysts are interesting candidates for alkaline water electrolysis also

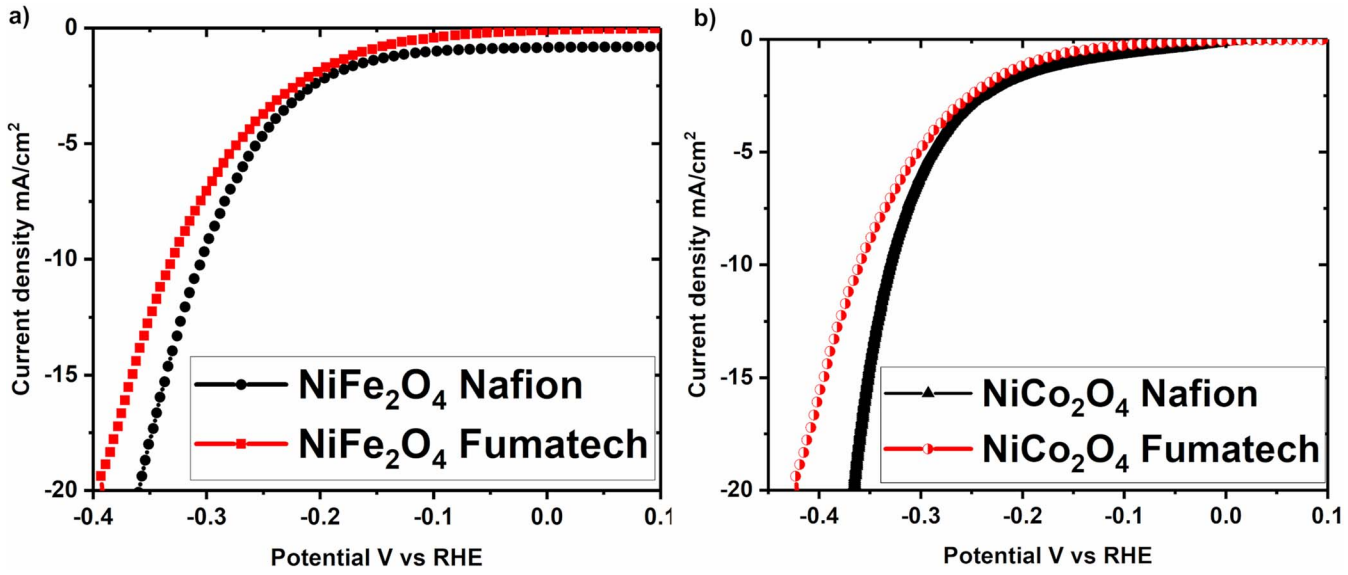

Figure 12. Linear sweep voltammetry for hydrogen evolution reaction normalized to the geometric surface area of a) $NiFe_2O_4$ and b) $NiCo_2O_4$ using Nafion and Fumatech binders. Data obtained in N_2-saturated 0.1 mol dm^{-3} KOH with a rotation rate of 1600 rpm.

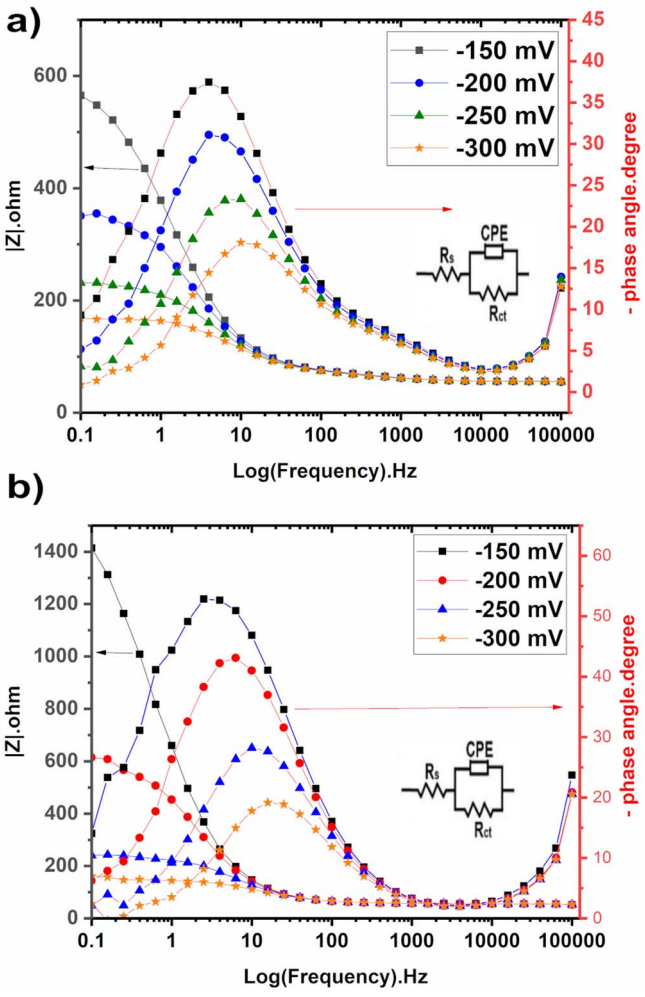

Figure 13. Electrochemical impedance spectroscopy (EIS) measurement: Bode plots of a) $NiFe_2O_4$ b) $NiCo_2O_4$ at different applied potentials (−150 to −300 mV vs. RHE) respectively.

from a durability perspective, and that long-term tests of their stability may be warranted in future research.

Conclusions

Ni, NiFe, and NiCo metal oxide catalysts of different compositions were synthesized by a simple co-precipitation method. The crystallite size and BET surface area change with composition. EDX, XRD and Raman analysis confirmed the presence of $NiFe_2O_4$ and $NiCo_2O_4$ spinel oxide phases in all the catalysts but the pure Ni sample, for which the structure is rocksalt NiO. Zeta potential measurements indicate some segregation of Ni at the catalyst surface.

The area-normalized, i.e. intrinsic catalytic activity of the catalysts for the HER is the same for all the catalysts in the series $Ni_{1+x}Fe_{2-x}O_4$ and $Ni_{1+y}Co_{2-y}O_4$ including the end member NiO. However, the cat-

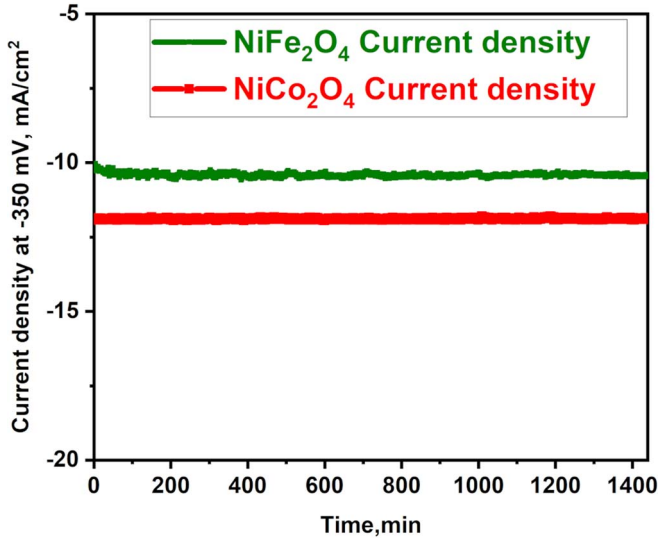

Figure 14. Chronoamperometry of $NiFe_2O_4$ and $NiCo_2O_4$ catalyst, data obtained in N_2-saturated 0.1 mol dm^{-3} KOH with a rotation rate of 1600 rpm using Nafion as a binder.

alytic activity per mass of the $Ni_{1+x}Fe_{2-x}O_4$ and $Ni_{1+y}Co_{2-y}O_4$ series catalysts changes through a modification of the electrochemical surface area. The composition of 33 mole-% Ni therefore displays the highest electrochemical activity due to lower crystallite size and largest electrochemical surface area. The similar activities for the area-normalized catalysts are consistent with their similar IEP values.

Tafel analysis indicates that the rate-determining step is the electrochemical adsorption of hydrogen (Volmer step). Fractional reaction orders with respect to OH^- can be interpreted in terms of double layer effects related to the pH-dependent surface charging mechanism. Application of the anion exchange ionomer Fumion FAA-3 in the catalytic layer led to a lower HER activity compared to an electrode with a Nafion ionomer. The performance of the combined ionomer-catalyst system may have significant implications for HER research in the AEM water electrolysis. Also, short term stability measurements indicate that $NiFe_2O_4$ and $NiCo_2O_4$ catalyts are stable under HER conditions.

Acknowledgment

This work was performed within HAPEEL project "Hydrogen Production by Alkaline Polymer Electrolyte Electrolysis" financially supported by the Research Council of Norway-ENERGIX program contract number 268019 and the INTPART project 261620. P.K.D. The Research Council of Norway is acknowledged for the support to the Norwegian Micro- and Nano-Fabrication Facility, NorFab, project number 245963/F50.

Appendix A. Derivation of Eq. 20

Taking the logarithm of Eq. 18 and differentiating with respect to the logarithm of OH^- gives the reaction order Ω_{OH^-},

$$\Omega_{OH^-} = \left.\frac{\partial \ln |i|}{\partial \ln [OH^-]}\right|_{E,T} = \left.\frac{\partial \ln \theta_H}{\partial \ln [OH^-]}\right|_{E,T} \quad [A1]$$

where $[OH^-]$ is the concentration of OH^-. Setting the rate of Reaction 11 to zero, which will be approximately the case if Reaction 12 is *rds*, gives

$$\theta_H = \frac{1}{1 + K_{-11}[OH^-]\exp(FE/RT)} \quad [A2]$$

where K_{-11} is $K_{-11} = k^0_{-11}/k^0_{11}$.

Then

$$\left(\frac{\partial \ln \theta_H}{\partial \ln [OH^-]}\right)_{E,T} = \left(\frac{[OH^-]}{\theta_H}\right)\left(\frac{\partial \theta_H}{\partial [OH^-]}\right)_{E,T} =$$

$$= -\frac{K_{-11}[OH^-]\exp(FE/RT)}{1 + K_{-11}[OH^-]\exp(FE/RT)} \quad [A3]$$

From Eq. 18 the Tafel slope can be calculated as

$$\frac{\partial \ln |i|}{\partial E} = b^{-1} = \frac{-\alpha F}{RT} + \frac{\partial \ln \theta_H}{\partial E} \quad [A4]$$

or since

$$\left(\frac{\partial \ln \theta_H}{\partial E}\right)_{[OH^-],T} = \left(\frac{1}{\theta_H}\right)\left(\frac{\partial \theta_H}{\partial E}\right)_{[OH^-],T} =$$

$$= -\frac{F}{RT}\frac{K_{-11}[OH^-]\exp(FE/RT)}{1 + K_{-11}[OH^-]\exp(FE/RT)} = \frac{F}{RT}\Omega_{OH^-} \quad [A5]$$

$$b^{-1} = \frac{F}{RT}\left(-\alpha + \Omega_{OH^-}\right) \quad [A6]$$

which corresponds to a similar equation derived by Tilak and Conway[47] for acid conditions.

Insertion of Eq. A2 into Eq. 18 gives

$$i = -\frac{2F\Gamma k^0_{12}\exp(-\alpha FE/RT)}{1 + K_{-11}[OH^-]\exp(FE/RT)} \quad [A7]$$

which predicts a Tafel slope and reaction order equal to $b = -RT/(1+\alpha)F$ (or $b = -2.303RT/(1+\alpha)F$ for a base-10 logarithm) and $\Omega_{OH^-} = -1$ at small negative values of E and $b = -RT/\alpha F$ and $\Omega_{OH^-} = 0$ large and negative E, consistent with Eq. A6.

Appendix B. Fractional Reaction Orders

If we assume that the potential in the rate expressions relate to the difference in potential in the catalyst surface, ϕ_M and that at the loci of adsorbates during electron transfer, $\phi_\ddagger$, the rate of the reaction in Eq. 11 becomes[48,68]

$$i = -2F\Gamma k^0_{11}(1-\theta_H)\exp\left[\frac{-\alpha F(\phi_M - \phi_\ddagger)}{RT}\right] \quad [B1]$$

If ϕ_S is the solution potential and we assume that ϕ_S is accessible through a reference electrode, the applied potential is $E = \phi_M - \phi_S$. Then, $\phi_M - \phi_\ddagger = E - (\phi_\ddagger - \phi_S)$. Insertion into Eq. B1 gives

$$i = -2F\Gamma k^0_{11}\exp\left(\frac{-\alpha FE}{RT}\right)\exp\left[\frac{-\alpha F(\phi_S - \phi_\ddagger)}{RT}\right] \quad [B2]$$

where we have also assumed that θ_H is negligible, consistent with the assumption of Reaction 11 being the *rds*. We write Eq. B2 as

$$i = -2F\Gamma k^0_{11}\exp\left(\frac{-\alpha FE}{RT}\right) f_{DL} \quad [B3]$$

where we have introduced the double-layer correction factor[68]

$$f_{DL} = \exp\left[\frac{-\alpha F(\phi_S - \phi_\ddagger)}{RT}\right] \quad [B4]$$

We assume acid-base equilibrium at the oxide surface, which leads to the following Nernst-type relation between the activity of protons at the surface, $a_{H^+_\ddagger}$, the activity of those in solution, $a_{H^+_*}$, and the potential difference $\phi_S - \phi_\ddagger$[48,49]

$$\frac{F}{RT}(\phi_S - \phi_\ddagger) = \ln\left(\frac{a_{H^+_\ddagger}}{a_{H^+_*}}\right) \quad [B5]$$

Insertion of Eq. B5 into Eq. B4 and the result, in turn, into Eq. B3, gives

$$i = -2F\Gamma k^0_{11}\left(\frac{a_{H^+_\ddagger}}{a_{H^+_*}}\right)^{-\alpha}\exp\left(\frac{-\alpha FE}{RT}\right) \quad [B6]$$

We now assume that $a_{H^+_\ddagger}$ does not vary appreciably with pH and absorb this quantity into the rate constant[48]

$$i = -2F\Gamma k^{0\prime}_{11} a^{\alpha}_{H^+_*}\exp\left(\frac{-\alpha FE}{RT}\right) \quad [B7]$$

where $k^{0\prime}_{11} = k^0_{11} a^{-\alpha}_{H^+_\ddagger}$. Applying the definition of reaction order to Eq. B7 gives the reaction order with respect to protons

$$\Omega_{H^+} = \left.\frac{\partial \ln |i|}{\partial \ln [H^+]}\right|_{E,T} = -\left.\frac{\partial \log |i|}{\partial (pH)}\right|_{E,T} = -\alpha \quad [B8]$$

which predicts that the slope of a plot of current on a logarithmic scale vs. pH is equal to $-\alpha$.

ORCID

Alaa Y. Faid https://orcid.org/0000-0003-3008-9774

References

1. J. Durst, A. Siebel, C. Simon, F. Hasché, J. Herranz, and H. A. Gasteiger, *Energy Environ. Sci*, **7**, 2255 (2014).
2. F. M. Sapountzi, G. M. Jose, C. J. Weststrate, H. O. A. Fredriksson, and J. W. Niemantsverdriet, *Prog. Energy Combust. Sci.*, **58**, 1 (2017).
3. W. Sheng, H. A. Gasteiger, and Y. Shao-Horn, *J. Electrochem. Soc.*, **157**, 11 (2010).
4. I. Vincent and D. Bessarabov, *Renew. Sustain. Energy Rev.*, **81**, 1690 (2018).
5. Q. Jia, E. Liu, L. Jiao, J. Li, and S. Mukerjee, *Curr. Opinion Electrochem.*, **12**, 209 (2018).
6. J. R. Varcoe, P. Atanassov, D. R. Dekel, A. M. Herring, M. A. Hickner, P. A. Kohl, A. R. Kucernak, W. E. Mustain, K. Nijmeijer, K. Scott, T. Xu, and L. Zhuang, *Energy Environ. Sci.*, **7**, 3135 (2014).
7. A. Y. Faid, A. O. Barnett, F. Seland, and S. Sunde, *Catalysts*, **8**, 614 (2018).
8. D. Chanda, J. Hnát, T. Bystron, M. Paidar, and K. Bouzek, *J. Power Sources*, **347**, 247 (2017).
9. D. Wang and D. Astruc, *Chem. Soc. Rev.*, **46**, 816 (2017).
10. M. Gong, W. Zhou, M. Tsai, j. Zhou, M. Guan, M. C. Lin, B. Zhang, Y. Hu, D. W. Yan, J. Yang, S. J. Pennycook, B. J. Hwang, and H. Dai, *Nat. Commun.*, **5**, 4695 (2014).
11. D. Chanda, J. Hnát, M. Paidar, J. Schauer, and K. Bouzek, *J. Power Sources*, **285**, 217 (2015).
12. M. A. Modestino, A. Kusoglu, A. Hexemer, A. Z. Weber, and R. A. Segalman, *Macromolecules*, **45**, 4681 (2012).
13. M. K. Bates, Q. Jia, N. Ramaswamy, R. J. Allen, and S. Mukerjee, *J. Phys. Chem. C*, **119**, 5467 (2015).

14. E. Veggetti, I. M. Kodintsev, and S. Trasatti, *J. Electroanal. Chem.*, **339**, 1 (1992).
15. A. J. Bard and L. R. Faulkner, *Electrochemical Methods Fundamentals and Application*, 2nd edition, p. 72, Wiley, (2001).
16. M. Silambarasan, P. S. Ramesh, and D. Geetha, *Spinel $NiCo_2O_4$ Nanostructures: Synthesis, Morphological, Optical and Electrochemical Properties in Recent Trends in Materials Science and Applications*, Ed: J. Ebenezar, Springer Proceedings in Physics, p. 219, (2017).
17. R. Nivetha, S. Chella, P. Kollu, S. K. Jeong, A. Bhatnagar, and N. G. Andrews, *J. Magn. Magn. Mater.*, **448**, 165 (2018).
18. K. Fominykh, G. Tok, P. Zeller, H. Hajiyani, T. Miller, M. Döblinger, R. Pentcheva, B. Rossitza, T. Bein, and D. Fattakhova-Rohlfing, *Adv. Funct. Mater.*, **27**, 1605121 (2017).
19. R. K. Sharma, H. Kumar, and A. Kumar, *RSC Adv.*, **5**, 43371 (2015).
20. A. Ahlawat and V. G. Sathe, *J. Raman Spectrosc.*, **42**, 1087 (2011).
21. J. Landon, E. Demeter, N. Inoglu, C. Keturakis, I. E. Wachs, R. Vasić, A. I. Frenkel, and J. R. Kitchin, *ACS Catal.*, **2**, 1793 (2012).
22. N. Mironova-Ulmane, A. Kuzmin, I. Steins, J. Grabis, I. Sildos, and M. Pärs, *J. Phys. Conf. Ser.* **93**, 1 (2007).
23. G. Liu, K. Wang, X. Gao, D. He, and J. Li, *Electrochim. Acta*, **211**, 871 (2016).
24. Z. Q. Liu, K. Xiao, Q. Z. Xu, N. Li, Y. Z. Su, H. J. Wang, and S. Chen, *RSC Adv.*, **3**, 4372 (2013).
25. H. K. Yadav, K. Sreenivas, V. Gupta, and R. S. Katiyar, *J. Raman Spectrosc.*, **40**, 381 (2009).
26. M. Gorlin, J. F. DeAraujo, H. Schmies, D. Bernsmeier, S. Dresp, M. Gliech, Z. Jusys, P. Chernev, R. Kraehnert, H. Dau, and P. Strasser, *J. Am. Chem. Soc.*, **139**, 2070 (2017).
27. L. A. DeFaria, M. Prestat, J. F. Koenig, P. Chartier, and S. Trasatti, *Electrochim. Acta*, **44**, 1481 (1998).
28. G. A. Parks, *Chem. Rev.*, **65**, 177 (1965).
29. M. Kosmulski, *Adv. Colloid Interface Sci.*, **238**, 1 (2016).
30. T. Mahmood, M. H. Saddique, A. Naeem, P. Westerhoff, S. Mustafa, and A. Alum, *Ind. Eng. Chem. Res.*, **50**, 10017 (2011).
31. S. Ardizzone and S. Trasatti, *Adv. Colloid Interface Sci.*, **64**, 173 (1996).
32. E. Guerrini and S. Trasatti, in *Catal. Sustain. Energy Prod.*, 235 (2009).
33. A. Kumar and S. Bhattacharyya, *ACS Appl. Mater. Interfaces*, **9**, 41906 (2017).
34. M. S. E. Houache, E. Cossar, and E. A. Baranova, *J. Power Sources*, **375**, 310 (2018).
35. G. Dong, M. Fang, J. Zhang, R. Wei, L. Shu, X. Liang, S. Yip, F. Wang, L. Guan, Z. Zheng, and J. C. Ho, *J. Mater. Chem. A.*, **5**, 11009 (2017).
36. C. Mahala and M. Basu, *ACS Omega*, **2**, 7559 (2017).
37. J. O. M. Bockris and T. Otagawa, *J. Electrochem. Soc.*, **131**, 290 (1984).
38. C. McCrory, S. Jung, J. C. Peters, and T. F. Jaramillo, *J. Am. Chem. Soc.*, **135**, 16977 (2013).
39. A. G. Oshchepkov, P. A. Simonov, O. V. Cherstiouk, R. R. Nazmutdinov, D. V. Glukhov, V. I. Zaikovskii, T. Y. Kardash, R. I. Kvon, A. Bonnefont, A. N. Simonov, V. N. Parmon, and E. R. Savinova, *Top. Catal.*, **58**, 181 (2015).
40. H. Chen and S. Trasatti, *J. Electroanal. Chem.*, **357**, 91 (1993).
41. T. Shinagawa, A. T. Garcia-Esparza, and K. Takanabe, *Sci. Rep.*, **5**, 13801 (2015).
42. M. Darab, A. O. Barnett, G. Lindbergh, M. S. Thomassen, and S. Sunde, *Electrochim. Acta*, **232**, 505 (2017).
43. F. Jaouen, G. Lindbergh, and K. Wiezell, *J. Electrochem. Soc.*, **150**, A1699 (2003).
44. A. G. Oshchepkov, A. Bonnefont, V. N. Parmon, and E. R. Savinova, *Electrochim. Acta*, **269**, 111 (2018).
45. Y. Dong, J. Dang, W. Wang, S. Yin, and Y. Wang, *ACS Appl. Mater. Interfaces*, **10**, 39624 (2018).
46. B. Zhang, H. Wang, H. Su, L. B. Lv, T. J. ZhaO, J. M. Ge, X. Wei, K. X. Wang, X. H. Li, and J. S. Chen, *Nano Res.*, **9**, 2606 (2016).
47. B. V. Tilak and B. E. Conway, *Electrochim. Acta*, **37**, 51 (1992).
48. A. H. Reksten, H. Thuv, F. Seland, and S. Sunde, *J. Electroanal. Chem.*, **819**, 547 (2018).
49. C. Angelinetta, M. Falciola, and S. Trasatti, *J. Electroanal. Chem.*, **205**, 347 (1986).
50. N. Krstajic and S. Trasatti, *J. Appl. Electrochem.*, **28**, 1291 (1998).
51. A. S. O. Gomes, N. Simic, M. Wildlock, A. Martinelli, and E. Ahlberg, *Electrocatalysis*, **9**, 333 (2017).
52. A. Carugati, G. Lodi, and S. Trasatti, *Mater. Chem.*, **6**, 255 (1981).
53. T. Shinagawa and K. Takanabe, *ChemSusChem*, **10**, 1318 (2017).
54. T. Shinagawa and K. Takanabe, *J. Phys. Chem. C*, **120**, 24187 (2016).
55. A. G. Vidales, K. Choi, and S. Omanovic, *Int. J. Hydrogen Energy*, **43**, 12917 (2018).
56. Y. Miao, L. Ouyang, S. Zhou, L. Xu, Z. Yang, Y. Zhuoyuan, X. Mingshu, and R. Ouyang, *Biosens. Bioelectron.*, **53**, 428 (2018).
57. S. Trasatti, *Adv. Electrochem. Sci. Eng.*, **ch. 1** 1 (2008).
58. S. Trasatti, *Hydrogen Evolution on Oxide Electrodes. In: Wellington T. C. (eds) Modern Chlor-Alkali Technology. Springer*, (1992).
59. S. Trasatti, *Croat. Chem. Acta*, **63**, 313 (1990).
60. E. Guerrini and S. Trasatti, *Russ. J. Electrochem.*, **42**, 1017 (2006).
61. M. A. Butler, *J. Electrochem. Soc.*, **125**, 228 (1978).
62. M. Schalenbach, F. D. Speck, M. Ledendecker, O. Kasian, D. Goehl, A. M. Mingers, B. Breitbach, H. Springer, S. Cherevko, and K. Mayrhofer, *Electrochim. Acta*, **259**, 1154 (2017).
63. N. Daems, T. Breugelmans, I. Vankelecom, and P. P. Pescarmona, *ChemElectroChem*, **5**, 119 (2018).
64. V. M. Nikolic, S. L. Maslovara, G. S. Tasic, T. P. Brdaric, P. Z. Lausevic, B. B. Radak, and M. P. Marceta Kaninski, *Appl. Catal. B Environ.*, **179**, 88 (2015).
65. A. Mukherjee, S. Chakrabarty, W. N. Su, and S. Basu, *Mater. Today Energy*, **8**, 118 (2018).
66. A. Lasia and A. Rami, *J. Electroanal. Chem.*, **294**, 123 (1990).
67. E. A. Franceschini, G. I. Lacconi, and H. R. Corti, *Int. J. Hydrogen Energy*, **41**, 3326 (2016).
68. J. Albery, *Electrode Kinetics*, Clarendon Press, Oxford, (1975).
69. S. Trasatti, *Chapter 43: Interfacial Electrochemistry of Conductive Oxides for Electrocatalysis in Interfacial electrochemistry : theory, experiment, and applications*, Ed: A. Wieckowski, p.769, Marcel Dekker, (1999).